# DEVELOPMENT OF SIMULATION MODELS FOR MORE ELECTRIC AIRCRAFT POWER SYSTEMS

By

Mauricio Céspedes

A Thesis Submitted to the Graduate
Faculty of Rensselaer Polytechnic Institute
in Partial Fulfillment of the
Requirements for the Degree of
MASTER OF SCIENCE
Major Subject: ELECTRICAL ENGINEERING

Approved:

_____

Jian Sun
Thesis Adviser

Rensselaer Polytechnic Institute
Troy, New York
December, 2009

# TABLE OF CONTENTS

# LIST OF TABLES

# LIST OF FIGURES

# ABSTRACT

Digital simulation is an important tool in the analysis of switching power converters due to their discontinuous dynamics and significant nonlinear behavior that even idealized models involve. In most of the situations, approximate models of the switching converters based on averaging theory are developed to give the necessary insight into the system behavior and serve as first step in control and stability analysis. It is common that in many cases even these approximate or averaged models are nonlinear, and digital simulation is also required in the analysis of their time domain response.

More Electric Aircraft (MEA) power systems are expected to exhibit a deep penetration of power-electronic based energy conversion systems. One of the main reasons is driven by the need for increased efficiency in the conditioning of electrical power. To some extend the increased flexibility and broadband control of the power-electronic conversion units is also a desirable characteristic in power system operation.

With the advent of switching power converters becoming major loads of the MEA power system, the need for new system analysis techniques devoted to the investigation of the impact of these new technologies has justified the development and implementation of simulation models of common power system components and switching power converters. These power converters are expected to have significant impact on system operation and control. This Thesis presents the development and implementation in Saber of representative models of the synchronous generator, the auto-transformer rectifier unit and the pulse-width modulated voltage-sourced converter for system simulation. The system architecture comprises a main electrical generator feeding constant amplitude AC voltage to the each of the power converters operating as rectified sources for variable frequency AC motor drives.

# CHAPTER 1  INTRODUCTION

This Thesis presents the development and implementation of digital simulation models of synchronous generators and switching power converters. Two types of models are developed: 1) full-order circuits that neglect most parasitic effects and 2) averaged models of switching power converters. Subsection 1.2 gives a brief review of the concept of the more eletrical aircraft power system. Subsection 1.2 provides an introduction to full-order modeling of each system component. Subsection 1.3 discusses the use of averaged models of the high-frequency switching converters. Subsection 1.4 gives an outline of the Thesis work.

## 1.1   More Electic Aircraft

Aircraft power systems are an example of high-performance systems required to generate and process electric power in more efficient ways. It shall be clear electrical efficiency translates into fuel efficiency which is not only desirable for reducing airplane operation costs but may also be required by environmental standards. One of the main objectives is to replace conventional pneumatic systems by electric driven hydraulic pumps in order to increase power conversion efficiency and reduce weight [14]. Examples of these systems being converted into "more electric" versions include air-conditioning and cabin presurization systems. In addtion to this goal, many of the electronic loads in the airplane may require dc power distribution, and also require efficient ac to dc electrical conversion circuits [15]. Power eletronic conversion systems offer the flexibility to operate in such hybrid ac-dc power system architecture. To some extend, the broadband control of these conversion units is also a desirable characteristic for power system operation. With the advent of switching power converters becoming major loads of the MEA power system, the need for new system analysis techniques devoted to the investigation of the impact of these new technologies has justified the development and implementation of simulation models of common power system components and switching power converters.

## 1.2   Full-Order Modeling

### 1.2.1   Synchronous Generator

Modeling of the synchronous machines [6-10] is widely documented. Typically [9] such models neglect the inter-winding capacitance, the hysteresis loss, the saturation of the magnetic circuits and any spatial harmonics. The effect of rotor circulating currents is represented by damper windings. The damper windings can be part of the machine construction or just a representation of the eddy currents in the rotor. Eddy currents are of special concern in high-speed turbogenerators [6], since they are constructed with solid-iron round rotors. Reference [10] showed that two or more circuits per axis are required to accurately model a round-rotor machine, while one damper circuit per axis suffices for a salient-pole machine. For the sake of simplicity, only one damper circuit per axis of the rotor will be modelled in this work.

The transformation of abc-coordinates into dq-coordinates has been commonly used in synchronous machine modeling. The purpose is to eliminate the angle-dependency of the machine inductances such that a time-invariant model can be developed. Furthermore, the resulting transformed model becomes linear if the frequency is assumed constant. A linear-time invariant model is desirable for control design and will serve as the basis for amplitude voltage control design.

### 1.2.2   Auto-Transformer Rectifier Units

Six pulse rectifiers draw large amount of harmonic currents that are not acceptable in many applications. Aerospace applications are typical high-performance systems requiring low-distortion ac-dc power conversion circuits [15]. Compared to high-frequency switching PWM converters, multi-pulse power rectifiers offer lower EMI emissions because they use low-frequency switching components. Moreover, when voltage regulation is not a major concern, multi-pulse converters offer a more reliable and low-cost solution [15,22].

Power transformer design is presented in detail in [16] and [17]. Reference [17] is of particular interest for this Thesis since it has been especially written for aerospace applications. For simplicity, symmetrical auto-transformer design topologies are favored [18-20], since the advantages of asymmetric designs (in terms of better rejection to leakage inductance variation [21]) falls outside the intended application of the models in this Thesis.

## 1.2.3 Voltage-Sourced Converter

Voltage-Sourced Converters (VSC) have been the subject of many publications. Implementation of representative converter models will only require to implement the general switching converter model [24] and its basic control approach [25]. Approximated converter models can be obtained by means of averaging theory [1-4] which will be further discussed in Subsection 1.3. The basic modeling approach will require to develop a discontinuous time model of the converter and applying next the averaging theory based on a time-scale separation of switching and other converter dyanmics. As in synchronous machine modeling, the dq-coordinate transformation is also useful in VSC control [25].

## 1.2.4 Variable Frequency Drives

The representative power-electronic enable loads this Thesis will implement are variable frequency drives for the permanent magnet (PM) motor and the wounded-rotor synchronous machine (SM). PM motors are commonly used in low power servodrives applications, since they have higher power density than comparable DC motors [27]. For modelling purposes, the PM synchronous machine can be consiedered a particular case of the wounded rotor type with constant excitation current. The modeling approach will begin by modeling the dynamics of the stator circuits of the machines which is combined with the VSC converter model to give a combined model of the motor drive. The control objective is to command the speed of the rotor by inflicting changes in the stator current.

## 1.3   Averaged Modeling

Switching power converter control is one of the main reasons for the development of averaged models that remove the time discontinuity of the switched-converter models. It was made clear in [2] that the techniques for controlling discontinuous systems are limited and they are not typically known by power electronics engineers. For control purposes, only the dynamic behavior of the average value or envelope of the system variables is relevant. Under these circumstances, Reference [4] explains modeling of the small switching ripple does not have much importance and the averaged models have the advantage of providing enough insight into converter behavior for controller design.

The limitation of averaged models to approximate the behavior of switching converters is a general concern. Reference [1] has presented a list of valuable conclusions to address these concerns, the one most relevant to this Thesis being that the averaged model does not represent only the small-signal dynamics of the converters but it also retains the large-signal behavior. Therefore large-signal disturbances such as start up and open-circuit transients can serve the purpose of evaluating the validity of the averaged models that will be developed in this Thesis.

The averaging method used here is based on the partitioning of fast and slow dynamics resulting from the notion of time scales for power converter analysis of [3] and [4]. The method consists in assuming a very high-switching frequency such that, in a Fourier series expansion of the fast switch dynamics, only the dc component is kept and the fast time-varying behavior is left out [3]. It is also possible to identify another time scale in electro-mechanical systems employing power electronic converters, such as the inverter-based variable frequency motor drives. In other words, the method is not restricted to the partition of the system into a single pair of time scales, as long as each group has considerably slower dynamics than the next.

## 1.4 Thesis Scope

The general objective of this Thesis is to implement in Saber representative models of the synchronous machine, the auto-transformer rectifier unit and the pulse-width modulated voltage-sourced converters for system simulation in an architecture that comprises a main electrical generator feeding constant amplitude AC voltage to the each of the power converters operating as rectified sources for variable frequency AC motor drives.

More specifically the models to develop and implement can be summarized as follows:

1) Synchronous generator for electromechanical energy conversion. The model shall include slow mechanical dynamics of the shaft as well as fast electromagnetic dynamics in the stator and rotor circuits. A representative excitation control system shall be developed to regulate the terminal voltage amplitude.

2) Auto-transformer rectifier for ac-dc electrical energy conversion. Symmetrical auto-transformer models for 18-pulse and 30-pulse direct rectification designs shall be presented. The models will include physic-based core models but can neglect parasitic losses in the core and switching components.

3) Pulse-width modulated voltage-sourced converter for bidirectional ac-dc electrical energy conversion. The two types of models to include are switching and averaged models of the two-level converter. The models shall be tested to evidence their correlation.

4) Variable frequency motor drive models for electromechanical energy conversion. Two-level voltage-source converter models shall be used to realize inverter-based motor drives as major loads for the ac-dc power converters. The motor models will include the permanent magnet (PM) motor and the wounded-rotor synchronous motor (SM).

# CHAPTER 2  SYNCHRONOUS MACHINE MODELING AND VOLTAGE CONTROL

This Chapter treats the modeling of the synchronous machine and its field circuit excitation control for amplitude voltage regulation. The physics-based behavior of the machine as a generator is modeled mathematically in dq-coordinates of the rotor for elimination of the time-varying inductances of stator and rotor circuits. The typical per unit specification of the machine parameters is revised and an example set is given for simulation case studies presented in this Thesis. The 2008 Saber simulation template dq3wrsyn is modified to fix modeling errors and to make available additional template variables for increased functionality. Amplitude voltage sensing techniques are revised and evaluated with actual simulations of the synchronous machine template with the purpose and outcome of implementing a representative excitation control circuit for the synchronous generator.

## 2.1   Dynamics of the Stator and Rotor

The abc-coordinate voltage equations modeling the stator and rotor circuits are as in [6]:

$$
\begin{bmatrix} v_a \\ v_b \\ v_c \\ v_{fd} \\ v_{kd} \\ v_{kq} \end{bmatrix} = \begin{bmatrix} -r_s i_a \\ -r_s i_b \\ -r_s i_c \\ r_{fd} i_{fd} \\ r_{kd} i_{kd} \\ r_{kq} i_{kq} \end{bmatrix} + \frac{\mathrm{d}}{\mathrm{d}t} \begin{bmatrix} \lambda_a \\ \lambda_b \\ \lambda_c \\ \lambda_{fd} \\ \lambda_{kd} \\ \lambda_{kq} \end{bmatrix}, \tag{1}
$$

where the flux linkages can be written in short form as

$$
\begin{bmatrix} \lambda_{abc} \\ \lambda_{FDQ} \end{bmatrix} = \begin{bmatrix} L_{ss}(\theta_r) & L_{sr}(\theta_r) \\ L_{sr}^T(\theta_r) & L_{rr} \end{bmatrix} \cdot \begin{bmatrix} -i_{abc} \\ i_{FDQ} \end{bmatrix}, \tag{2}
$$

and $\theta_r$ is the angle of the rotor. Note for the stator circuits the positive-current direction is taken as leaving the windings known as generator convention which is followed in [6], but for the rotor circuits is taken as going into the rotor-windings. Another equally valid convention changes the stator current polarity and is known as motor convention followed in [7].

The angle of the rotor is measured from the magnetic axis of phase a to the q axis of the rotor which leads the d axis by 90 degrees as depicted in Fig. 2. 1.
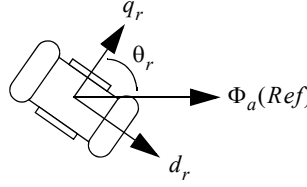


**Fig. 2. 1.** Illustration of the dq-coordinates of the rotor.

In the general case, the flux linkages involving the stator circuits are angle dependent since their reluctance changes as the rotor revolves. However, the first submatrix in (2) $L_{ss}(\theta_r)$ known as the stator-self inductance and given by

$$
\begin{bmatrix}
L_{ls} + L_A - L_B\cos(2\theta_r) & -\dfrac{L_A}{2} - L_B\cos 2\left(\theta_r - \dfrac{\pi}{3}\right) & -\dfrac{L_A}{2} - L_B\cos 2\left(\theta_r + \dfrac{\pi}{3}\right) \\
-\dfrac{L_A}{2} - L_B\cos 2\left(\theta_r - \dfrac{\pi}{3}\right) & L_{ls} + L_A - L_B\cos 2\left(\theta_r - \dfrac{2\pi}{3}\right) & -\dfrac{L_A}{2} - L_B\cos(2\theta_r) \\
-\dfrac{L_A}{2} - L_B\cos 2\left(\theta_r + \dfrac{\pi}{3}\right) & -\dfrac{L_A}{2} - L_B\cos(2\theta_r) & L_{ls} + L_A - L_B\cos 2\left(\theta_r + \dfrac{2\pi}{3}\right)
\end{bmatrix}, \quad (3)
$$

losses its angle dependency in the case of round-rotor machines, because as will be evident later, in that case $L_B$ is equivalent to zero. The rest of the submatrices are expanded as follows, for the stator-to-rotor mutual flux linkages

$$\lambda_{abc}] = \begin{bmatrix} L_{sfd}\sin\theta_r & L_{skd}\sin\theta_r & L_{skq}\cos\theta_r \\ L_{sfd}\sin\left(\theta_r - \dfrac{2\pi}{3}\right) & L_{skd}\sin\left(\theta_r - \dfrac{2\pi}{3}\right) & L_{skq}\cos\left(\theta_r - \dfrac{2\pi}{3}\right) \\ L_{sfd}\sin\left(\theta_r + \dfrac{2\pi}{3}\right) & L_{skd}\sin\left(\theta_r + \dfrac{2\pi}{3}\right) & L_{skq}\cos\left(\theta_r + \dfrac{2\pi}{3}\right) \end{bmatrix} \cdot [i_{FDQ}, \tag{4}$$

and the rotor self flux linkages

$$[\lambda_{FDQ}] = \begin{bmatrix} L_{lfd} + L_{mfd} & L_{fdkd} & 0 \\ L_{fdkd} & L_{lkd} + L_{mkd} & 0 \\ 0 & 0 & L_{lkq} + L_{mkq} \end{bmatrix} \cdot [i_{FDQ}]. \tag{5}$$

The last equation is not angle dependent because as seen from an fixed observer in the rotor, the stator resembles a smooth surface without variable reluctance.

## 2.1.1   Rotor-Oriented Transformation

In order to remove the angle dependency and time-varying behavior of the inductance submatrices, a dq0-coordinate transformation aligned and synchronously rotating with the rotor (see Fig. 2. 1) is applied to the abc-coordinates as follows

$$\begin{bmatrix} x_d \\ x_q \\ x_0 \end{bmatrix} = \sqrt{\dfrac{2}{3}} \begin{bmatrix} \sin\theta_r & \sin(\theta_r - 2\pi/3) & \sin(\theta_r + 2\pi/3) \\ \cos\theta_r & \cos(\theta_r - 2\pi/3) & \cos(\theta_r + 2\pi/3) \\ \dfrac{1}{\sqrt{2}} & \dfrac{1}{\sqrt{2}} & \dfrac{1}{\sqrt{2}} \end{bmatrix} \begin{bmatrix} x_a \\ x_b \\ x_c \end{bmatrix}. \tag{6}$$

As given above the transformation is power invariant, and as explained in [8] this definition makes more intuitive the generator's power equation, the rotor-to-stator transformation and per unit conversion, and it differs from the Park's transformation used in [6].

For simplicity, apply first the transformation to the stator-self inductance matrix in (3) giving

$$\left[\lambda_{dq0}\right] = \begin{bmatrix} L_{ls} + L_{md} & 0 & 0 \\ 0 & L_{ls} + L_{mq} & 0 \\ 0 & 0 & L_{ls} \end{bmatrix} \left[-i_{dq0}\right], \tag{7}$$

where $L_{md} = 3(L_A + L_B)/2$ and $L_{mq} = 3(L_A - L_B)/2$ are defined as the direct and quadrature axis inductances respectively. Transformation of the stator-rotor mutual inductance in (4) gives

$$\left[\lambda_{dq0}\right] = \begin{bmatrix} \sqrt{\frac{3}{2}} L_{sfd} & \sqrt{\frac{3}{2}} L_{skd} & 0 \\ 0 & 0 & \sqrt{\frac{3}{2}} L_{skq} \\ 0 & 0 & 0 \end{bmatrix} \left[i_{FDQ}\right], \tag{8}$$

and it is clear the rotor angle dependency has been removed. Now transform the voltage equations in (1) giving

$$\begin{bmatrix} v_{dq0} \\ v_{FDQ} \end{bmatrix} = \begin{bmatrix} -r_s i_d \\ -r_s i_q \\ -r_s i_0 \\ r_{fd} i_{fd} \\ r_{kd} i_{kd} \\ r_{kq} i_{kq} \end{bmatrix} + \begin{bmatrix} 0 & -\omega_r & 0 \\ \omega_r & 0 & 0 \\ 0 & 0 & 0 \end{bmatrix} \left[\lambda_{dq0}\right] + \frac{\mathrm{d}}{\mathrm{d}t} \begin{bmatrix} \lambda_{dq0} \\ \lambda_{FDQ} \end{bmatrix}, \tag{9}$$

where the second term has the speed of the rotor as coefficient and is a result of transforming the derivative of abc-coordinate flux linkages. Note equations (1)-(5) have been reduced to (7)-(9) and the latter does not have any time-varying coefficients if the rotor speed is considered constant. A further simplification in terms of parameter specification is possible if stator and rotor base impedances are related to each other as will be presented in the next subsection.

9

## 2.1.2 Stator and Rotor Base Impedances

In power systems it is a common practice to express equipment parameters in per unit quantities and in order to input these parameters correctly in the digital simulation environment, careful analysis of the base in which they are handled is very important. Furthermore, matrices (7) and (8) as compared to (3) and (4) are clearly simplified by the rotor-oriented transformation in the reference frame for the stator-equations, but the parametrization of the model can be simplified further by the definition of "convenient bases" [8] for stator and rotor circuits. A typical selection for the stator base quantities is given in Table 2. 1.

**Table 2. 1. Typical Stator Base Specification**

| Base | Symbol | Description and units |
|---|---|---|
| Power Base | $S_B$ | Stator rated power, 3-ph MVA |
| Voltage Base | $V_B$ | Stator rated voltage, line-line kV |
| Speed | $\omega_B$ | Generator rated speed, electrical rad/s |

From those definitions in Table 2. 1 all other stator-related bases can be obtained, for example, $t_B = 1/\omega_B$, $I_B = S_B/V_B$, $Z_B = V_B/I_B$ and $L_B = V_B/(I_B\omega_B)$ . Saber's base definitions in the 2003 release differ from those in Table 2. 1, in that the power base is the rated 3-ph power in kVA, the base voltage is the peak rated line-to-neutral voltage and the base current is the peak rated current. However, it can be shown the impedance base is numerically equivalent to one presented here.

For the definition of rotor-base quantities, and in general for the normalization of circuits coupled electromagnetically, Reference [8] asserts it is essential to select the same volt-ampere and time bases, while the third base quantity is flexible. However, its selection is still important since the volt-ampere rating of the stator is much larger than that of the rotor, and per unit quantities may result very small. From the following definitions:

$L_{ld} + L_{md} = L_d$, $L_{lfd} + L_{mfd} = L_{fd}$, $L_{lkd} + L_{mkd} = L_{kd}$, $L_{lkq} + L_{mkq} = L_{kq}$, the results in Table 2. 2 are proven in [8].

**Table 2. 2. Example Rotor Base Specification**

| Circuit | Base Voltage | Base Current | Base Impedance | Turns ratio |
|---|---|---|---|---|
| Field | $V_{fd,B} = k_{fd}V_B$ | $I_{fd,B} = k_{fd}^{-1}I_B$ | $Z_{fd,B} = k_{fd}^2 Z_B$ | $k_{fd} = \sqrt{\dfrac{3}{2}\dfrac{L_{sfd}}{L_{md}}}$ |
| d-axis damper | $V_{kd,B} = k_{kd}V_B$ | $I_{kd,B} = k_{kd}^{-1}I_B$ | $Z_{kd,B} = k_{kd}^2 Z_B$ | $k_{kd} = \sqrt{\dfrac{3}{2}\dfrac{L_{skd}}{L_{md}}}$ |
| q-axis damper | $V_{kq,B} = k_{kq}V_B$ | $I_{kq,B} = k_{kq}^{-1}I_B$ | $Z_{kqB} = k_{kq}^2 Z_B$ | $k_{kq} = \sqrt{\dfrac{3}{2}\dfrac{L_{skq}}{L_{mq}}}$ |

The turns ratios in Table 2. 2, when applied to the synchronous generator equations relating stator-to-rotor inductances give the following results

$$
\left[\lambda_{dq0}\right] = \begin{bmatrix} L_d & 0 & 0 \\ 0 & L_q & 0 \\ 0 & 0 & L_{ls} \end{bmatrix} \left[-i_{dq0}\right] + \begin{bmatrix} L_{md} & L_{md} & 0 \\ 0 & 0 & L_{mq} \\ 0 & 0 & 0 \end{bmatrix} \left[i_{FDQ}{'}\right]
\tag{10}
$$

and

$$
[\lambda_{FDQ}{'}] = \begin{bmatrix} L_{md} & 0 & 0 \\ L_{md} & 0 & 0 \\ 0 & L_{mq} & 0 \end{bmatrix} \left[-i_{dq0}\right] + \begin{bmatrix} L_{lfd}{'} + L_{md} & L_{md} & 0 \\ L_{md} & L_{lkd}{'} + L_{md} & 0 \\ 0 & 0 & L_{lkq}{'} + L_{mq} \end{bmatrix} [i_{FDQ}{'}] , \tag{11}
$$

where the superscript prime denotes quantities referred to the stator base. If these turns ratios are also applied to the voltage equations, the result for the complete generator model is as follows

11

$$v_d = -r_s i_d - \omega_r[-L_q i_q + L_{mq}(i_{kq}')] + \frac{d}{dt}[-L_d i_d + L_{md}(i_{fd}' + i_{kd}')]$$

$$v_q = -r_s i_q + \omega_r[-L_d i_d + L_{md}(i_{fd}' + i_{kd}')] + \frac{d}{dt}[-L_q i_q + L_{mq}(i_{kq}')]$$

$$v_0 = -r_s i_0 + \frac{d}{dt}[-L_{ls} i_0]$$

$$v_{fd}' = r_{fd}' i_{fd} + \frac{d}{dt}[-L_{md} i_d + (L_{lfd}' + L_{md}) i_{fd}' + L_{md} i_{kd}']$$

$$v_{kd}' = r_{kd}' i_{kd}' + \frac{d}{dt}[-L_{md} i_d + L_{md} i_{fd}' + (L_{lkd}' + L_{md}) i_{kd}']$$

$$v_{kq}' = r_{kq}' i_{kq}' + \frac{d}{dt}[-L_{mq} i_q + (L_{lkq}' + L_{mq}) i_{kq}']$$

(12)

The adoption of a per unit system will depend on the type of dq-coordinate transformation adopted in the analysis. As noted before, Saber and [6] have adopted different base definitions and a different dq0-coordinate transformation matrix for the stator circuits. However, both methods give the same generator model in (12) where the rotor circuit resistances and leakage inductances as referred to the stator are also equivalent to the definitions in here.

## 2.2  Dynamics of the Shaft

The inertial equation governing the rotor dynamics is given by

$$T_m = T_e + B\omega_r + J\frac{d\omega_r}{dt}, \tag{13}$$

where $T_m$ is the mechanical torque, $T_e$ is the electromagnetic torque, $B$ is the damping constant, $\omega_r$ is the speed and $J$ is the inertia. Note in the generator convention, the mechanical torque represents the turbine force driving the (counter) electromagnetic torque and the shaft's inertial and damping torques that are always in opposition to the force causing movement.

The electromagnetic torque is obtained from a power balance equation. The output power of the generator in dq-coordinate modeling is obtained from

$$P_{gen} = v_d i_d + v_q i_q. \tag{14}$$

Upon introduction of $v_d$ and $v_q$ given in (12) one obtains

$$P_{gen} = -r_s i_d^2 - r_s i_q^2 + i_d \frac{\mathrm{d}}{\mathrm{d}t}(\lambda_d) + i_q \frac{\mathrm{d}}{\mathrm{d}t}(\lambda_q) + \omega_r \lambda_d i_q - \omega_r \lambda_q i_d, \tag{15}$$

where the first two terms correspond to the resistive losses in the stator windings, the derivative of the flux linkages are the energy storage in the magnetic flux of the machine and the speed related terms give the power transmitted through the airgap. These last two terms give the machine electromagnetic torque

$$T_e = \lambda_d i_q - \lambda_q i_d. \tag{16}$$

## 2.3   Saber Template Modifications

An un-encrypted version of the synchronous machine template *dq3wrsyn* in Saber's 2008 release was facilitated as part of a joined cooperation with Synopsys R&D Division. After revising the template code lines it was determined the template made an inconsistent use of the generator and motor conventions in the machine voltage equations. The minus sign in the coefficients of the dq0-coordinate stator currents in (12) is a result of the generator convention. Correction of the template was done adopting the generator convention used here and the necessary modifications in the rest of the template were done accordingly.

One important modification is introduced in the machine torque dynamics. In the Saber simulator environment, a positive torque intends to cause an increase in the mechanical speed, while a negative torque has the opposite effect. From this definition, the shaft dynamics in (13) need to be introduced in MAST[1] language as follows

$$\text{tq\_Nm(shaft)} \mathrel{+}= \text{-tq\_gen - d\_by\_dt(J*wr) - B*wr} \tag{17}$$

where tq_gen is the electromagnetic torque as given by (16).

---

1.  For a complete tutorial in MAST language consult [12]

Additional functionality of the template was introduced by making the rotor angle of the machine available for external use within simulator schematics. This information is particularly useful in the vector control of machine drives for alignment of the stator magnetic field or in the validation of frequency domain models of the machine voltage equations for terminal voltage control. The modification is realized by declaring the new variable for external use in the header and local declarations sections of the template. The new variable is assigned the value of the rotor angle in the equations section of the template. Finally the schematic symbol is modified to accommodate for the new available information, and Fig. 2. 2 depicts the modified template symbol.
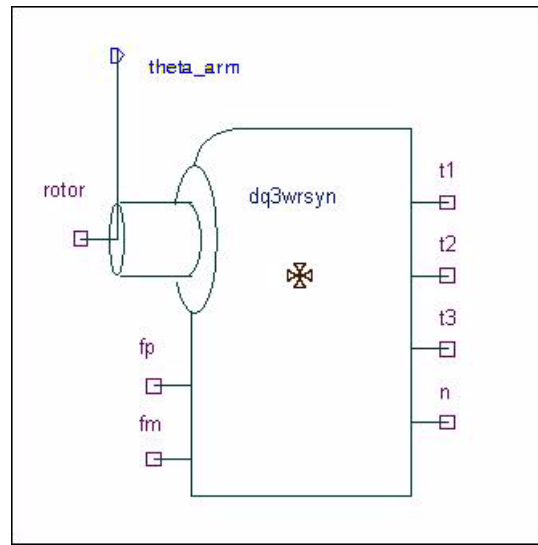


**Fig. 2. 2.** Schematic symbol of the synchronous machine template after modifications to include the rotor angle information

## 2.4  Example Parameter Specification

Representative parameters have been estimated for simulation of a synchronous generator rated for 250 kW, 235 $V_{RMS}$ (line-neutral) and 400 Hz and are listed in Table 2. 3. The parameters represent a solid iron turbogenerator since the d- and q-axis synchronous reactances are identical and both subtransient reactances and time-constants are also expected to be similar. The stator resistance is approximated based on 3% power loss in

the windings. Generator inertia, damping constant and number of poles are also the typical values observed in turbogenerators [8]. The Saber template prompts for $\tau_q'$ although the model only includes one damper winding in the q-axis (hence it is zero, and in fact any number can be specified since it is not used through the template routine).

**Table 2. 3. Parameters for 250 kW (P.F. 0.85), 235 V$_{RMS}$ (L-N) and 400 Hz turbogenerator**

| Parameter | Value | Unit |
|:---:|:---:|:---:|
| $x_{ls}$ | 0.09 | pu |
| $x_0$ | 0.09 | pu |
| $x_d$ | 1.10 | pu |
| $x_q$ | 1.10 | pu |
| $x_d'$ | 0.132 | pu |
| $x_q'$ | 0.264 | pu |
| $x_d''$ | 0.095 | pu |
| $x_q''$ | 0.095 | pu |
| $\tau_d'$ | 0.180 | s |
| $\tau_q'$ | 0 | s |
| $\tau_d''$ | 0.006 | s |
| $\tau_q''$ | 0.006 | s |
| $r_s$ | 0.0194 | $\Omega$ |
| $J$ | 700 | kg m$^2$ |
| $B_m$ | 2 | N m rad/s |
| $p$ | 2 | poles |

Typically, the generator impedances are given in manufacturer's base impedance which in general is equivalent to the template base so that no base conversion is required. However, the template does convert the per unit parameters to the SI parameters for simulation of the model in (12). Therefore caution shall be exercised to check the numerical results of the conversion. Cases have been observed (see for example the 62.5 MVA turbogenerator from the appendix of [8]) where the subtransient inductance of the d-axis is

smaller than the leakage inductance (0.102 pu and 0.113 pu respectively), yielding a negative value for the approximated leakage inductance of the d-axis damper. In general, all sub-transient inductances shall be larger than the leakage inductance.

## 2.5   Voltage Sensing Methods

For synchronous generators, voltage control is interpreted as amplitude control since the sine-wave is inherently created by the generator physical construction and the assumption of sinusoidally distributed windings. The response of the terminal voltage to the change in the excitation voltage can be obtained from the model in (12). Since this is a rotor-oriented transformation, the angle information from the modified template in Fig. 2. 2 can be used. The frequency domain response of the d axis voltage to a perturbation in the field voltage excitation is given by

$$G_{vd}^{r}(s) \; =$$

$$\frac{sL_{md}(r_{kd} + sL_{lkd})}{r_{fd}[r_{kd} + s(L_{lkd} + L_{md})] + s[L_{md}(r_{kd} + sL_{lkd}) + L_{lfd}(r_{kd} + s(L_{lkd} + L_{md}))]} \quad , \qquad (18)$$

and the q axis voltage response to the perturbation is given by

$$G_{vq}^{r}(s) \; =$$

$$\frac{\omega_{r}L_{md}(r_{kd} + sL_{lkd})}{r_{fd}[r_{kd} + s(L_{lkd} + L_{md})] + s[L_{md}(r_{kd} + sL_{lkd}) + L_{lfd}(r_{kd} + s(L_{lkd} + L_{md}))]} \quad , \qquad (19)$$

where the prime superscript from the stator referred parameters has been dropped for simplicity.

Fig. 2. 3 shows the frequency response plots of (18) and (19) together with Saber simulation results, note at low frequencies the dominant component is the q-axis response, while the d-axis component becomes more significant above the rotor angular speed.
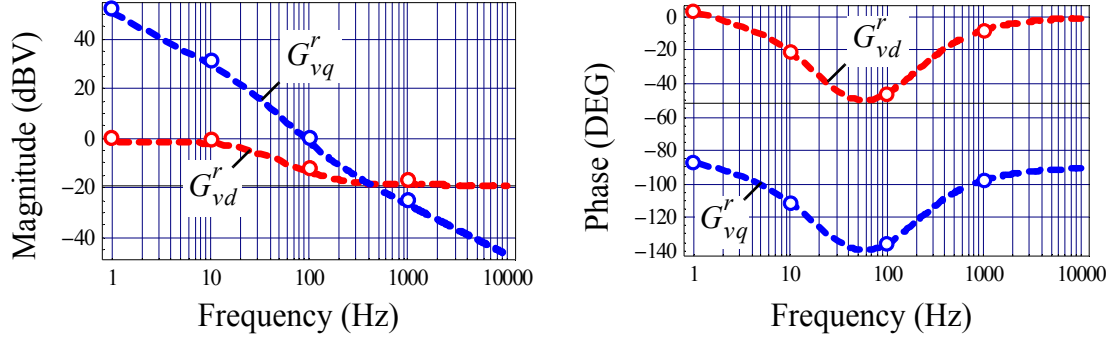
**Fig. 2. 3.** Frequency response plot of terminal voltage response in open-circuit to excitation perturbation.

## 2.5.1 Stator-Oriented Transformation

A dq-coordinate transformation synchronously rotating with the generator terminal voltage has the ability of extracting the voltage amplitude. As shown in Fig. 2. 4 a phase-lock loop technique based on the dq-transformation can be used to generate the angle reference for the transformation by locking the q-axis voltage with the phase a voltage, while extracting the voltage amplitude in the d-axis component.
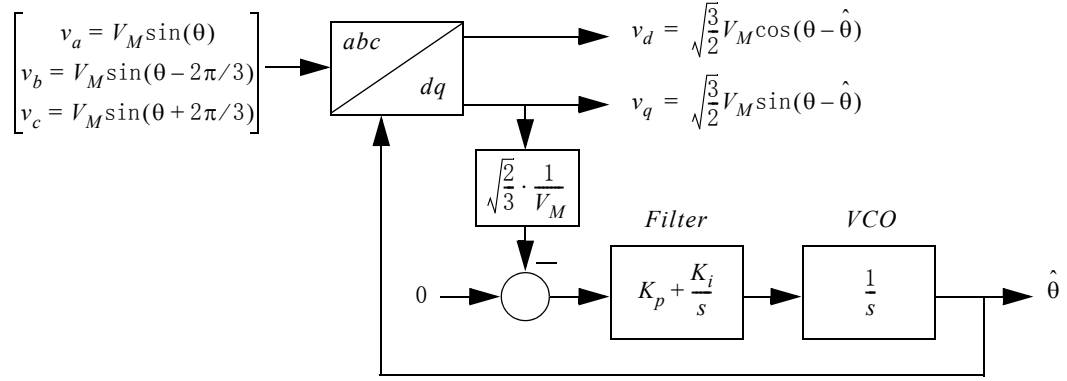


**Fig. 2. 4.** Functional diagram of dqPLL for angle and amplitude detection of three-phase voltages.

The second-order closed loop transfer function associated with the dqPLL is

$$\frac{\delta_e(s)}{\delta_{ref}(s) - \delta_e(s)} = \frac{2\zeta\omega_n s + \omega_n^2}{s^2 + 2\zeta\omega_n s + \omega_n^2}, \tag{20}$$

17

where $K_p = 2\zeta\omega_n$ and $K_i = \omega_n^2$. A trade-off in the design of the locking bandwidth is harmonic voltage noise affecting the angle acquisition.

The dqPLL is intended to lock on the condition $\theta - \hat{\theta} = 0$, but it has always been the case that it locks to $\theta - \hat{\theta} = \pi$, another possible equilibrium point for the dqPLL in Fig. 2. 4. Under the latter condition, the d-axis voltage of the stator-oriented transformation will resemble $(-G_{vq}^r)$ as corroborated in Fig. 2. 5, while the q-axis voltage will be kept at zero.
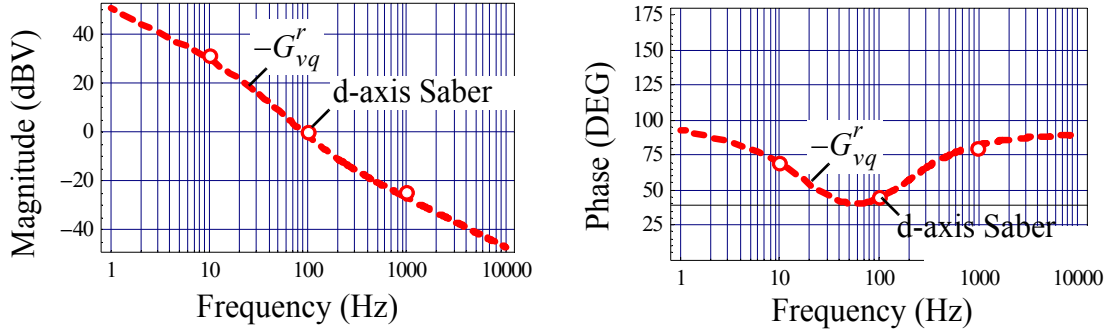


**Fig. 2. 5.** Frequency response plot of synchronous machine terminal voltage response in the d-coordinate of a stator-oriented transformation using a dqPLL.

### 2.5.2 Rectified Voltage Sensor

Another common approach for acquisition of voltage amplitude is from direct rectification of the three-phase voltages. A simplified model of the generator at low-frequencies assumes the major contribution to the voltage induced in the stator by the field circuit comes from the speed related term, that is the q-axis voltage in the rotor-oriented model, giving the transfer function

$$G_{vo}(s) =$$

$$\frac{k_0 \cdot [\omega_r L_{md}(r_{kd} + sL_{lkd})]}{r_{fd}[r_{kd} + s(L_{lkd} + L_{md})] + s[L_{md}(r_{kd} + sL_{lkd}) + L_{lfd}(r_{kd} + s(L_{lkd} + L_{md}))]} \quad , \quad (21)$$

where $k_0 = 2N\sin(\pi/N)/\pi$ is the gain of the N-phase rectifier.

The rectified voltage is filtered by an LC network with a resonance frequency sufficiently above the voltage controller bandwidth such that no additional phase lag is introduced. Here it has been assumed $L = 2.5$ mH, $C = 10$ μF, and $R = 5$ kΩ, such that consuming only 60 W of power the frequency response of the output voltage to a perturbation in the field voltage is shown in Fig. 2. 6.
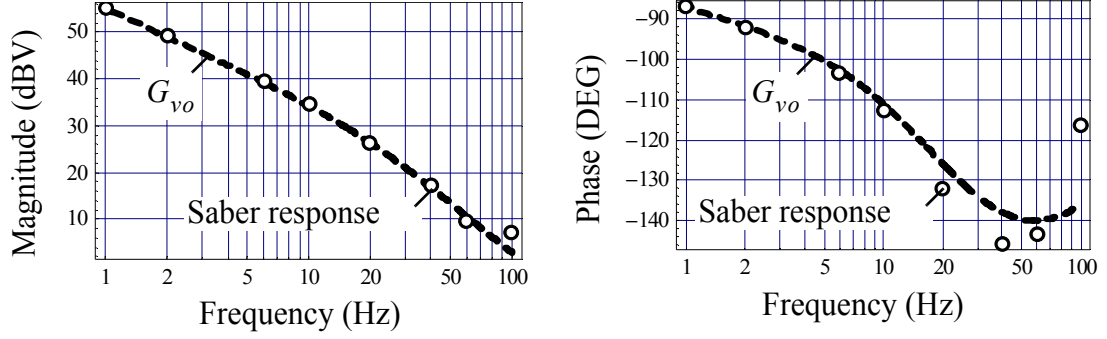


**Fig. 2. 6.** Frequency response plot of 6-pulse rectifier voltage response to harmonic perturbations in the generator field excitation circuit.

## 2.6 Excitation Control

The dqPLL is the voltage sensing technique implemented hereafter, and is preferred because the model is valid over a wider frequency range when compared to the simple rectifier technique. Fig. 2. 7 shows the implementation in Saber of the dqPLL together with the symbol that has been created for its application in system simulations. As explained before, the d-axis voltage carries the information of the voltage amplitude, and the gain of the circuit is adjusted after the abc-to-dq block in order to have $V_M$ at the output (not $(\sqrt{3/2})V_M$). Note that due to the locking $\theta - \hat{\theta} = \pi$, in order to obtain the *phase a* angle information at the output, $\pi$ is substracted from the output of the schematic.

From the voltage transfer function in (19), a PI compensator is sufficient for eliminating the steady-state error and providing the necessary phase compensation

$$H_i(s) = \left(K_P + \frac{K_I}{s}\right)\left(\frac{1}{1 + s/\omega_p}\right).$$ (22)
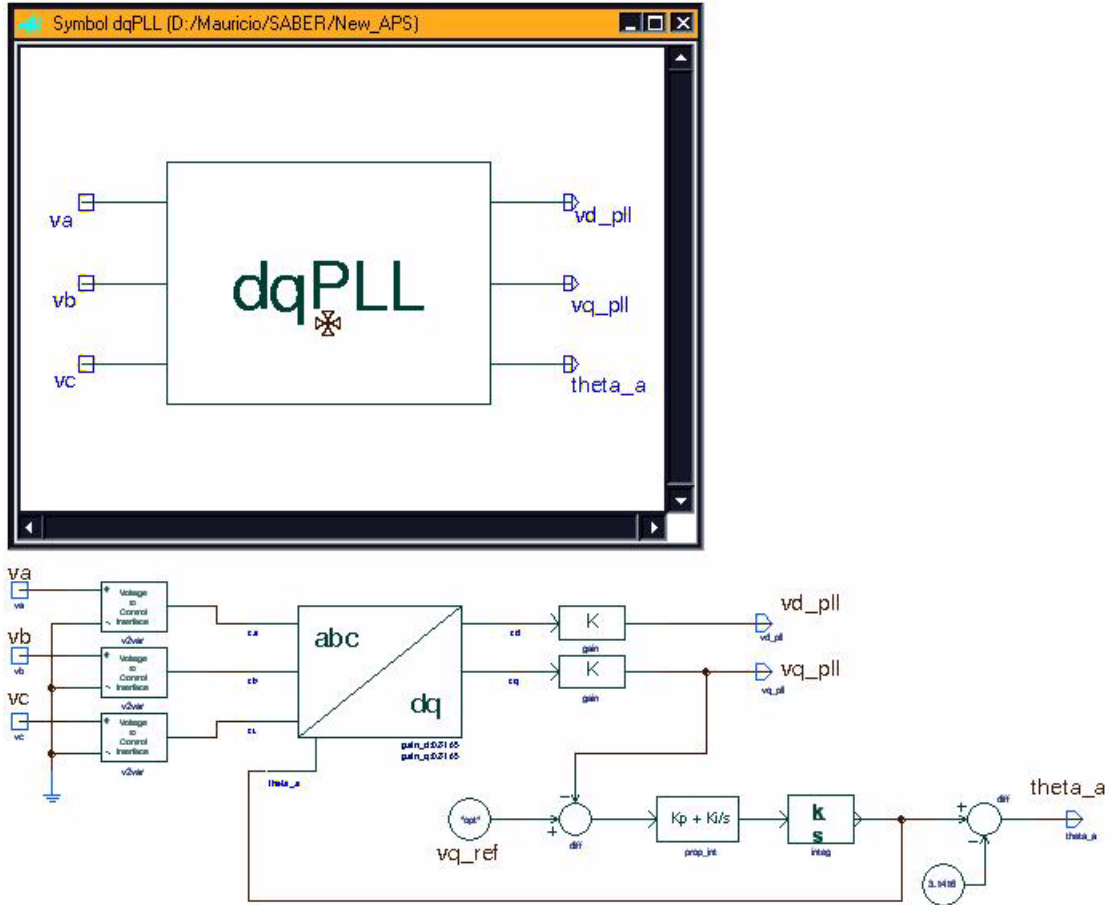
**Fig. 2. 7.** Symbol and schematic implementation of dqPLL in Saber

An additional pole at 10 times the crossover frequency prevents noise from disturbing the regulation. The proposed design for 3.67 Hz crossover frequency and 54 degrees of phase margin requires setting $K_P = 0.01$, $K_I = 0.1$ and $\omega_p = 2\pi \cdot 40$.

The exciter circuit implemented in Saber is shown in Fig. 2. 8. It receives the error signal from a comparator and represents the exciter type IEEE-ST1A [13]. The time constant associated with the actual application of field voltage is neglected for the very low bandwidth of the regulator, and a limiter has been added and set to 200% of the rated full-load exciter voltage.
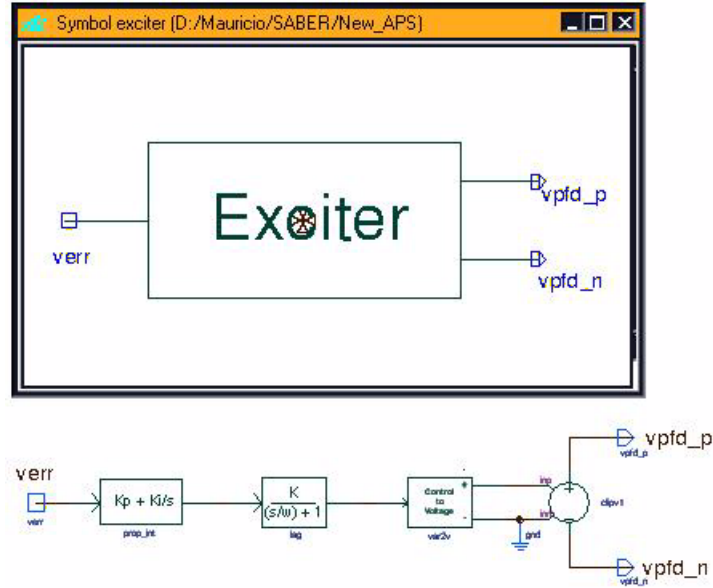
**Fig. 2. 8.** Symbol and schematic implementation of representative exciter IEEE-ST1A in Saber

The response of the excitation circuit to a sudden load increase of 250 kW is depicted in Fig. 2. 9 together with the *phase a* magnitude as reflected in $v_{dpll}$. The exciter increases the voltage in the field circuit in response to the sudden voltage drop while the limiter avoids the excitation from becoming negative at the overshoot of phase voltage. Steady-state is reached after 300 cycles.
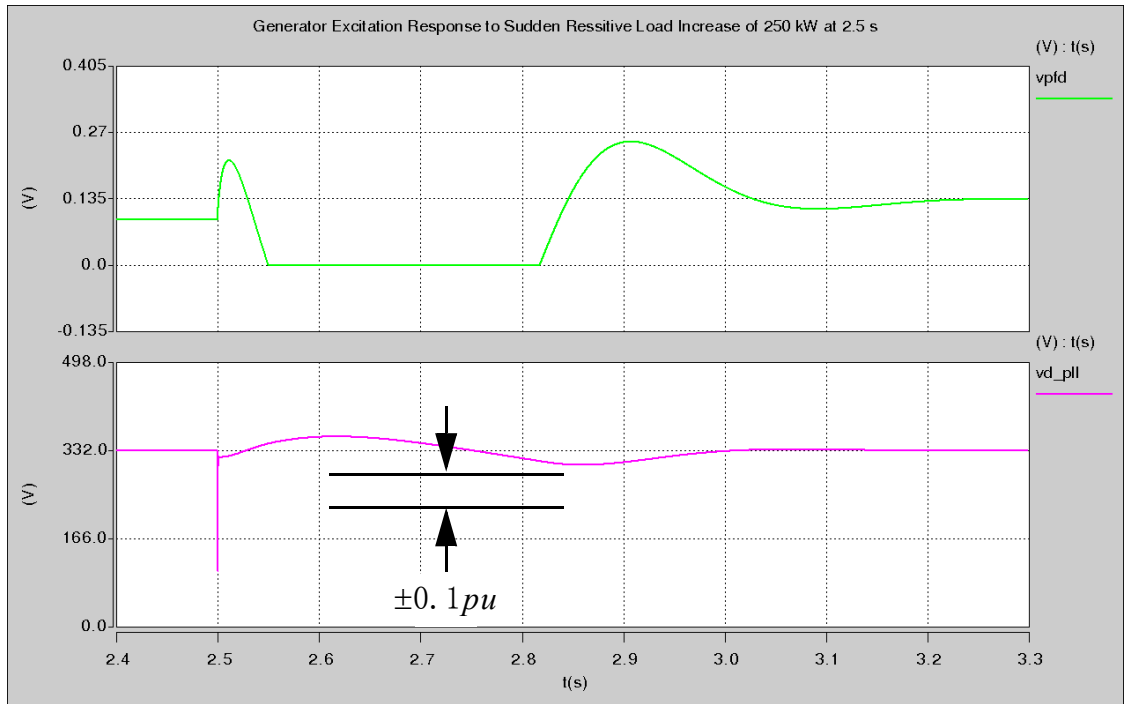
**Fig. 2. 9.** Time domain response of generator excitation to sudden resistive load increase of 250 kW at 2.5 s

## 2.7  Conclusions

The dq-coordinate modeling of the synchronous machine stator and rotor circuits including one damper circuit per rotor axis has been presented. The rotor-oriented transformation is introduced to remove the rotor-angle dependency of the machine inductances. Equation (12) is the main outcome of the modeling process where a generator convention has been adopted. It is worth noting the model is linear under the assumption of constant rotor speed.

The model of the shaft dynamics in (13) also adopts the generator convention since mechanical torque is balanced by the electromagnetic, inertial and damping torques. In order to model the electromagnetic torque, a power balance equation is used to give the expression in (16). This equation differs from the one in Krause [6] (5.6-3) since the latter uses a different dq-coordinate transformation and in the models the general case of a number P of pole pairs.

In the scenario of constant rotor speed, the machine voltage equations represent a linear-time-invariant dynamic model of the stator dq-coordinate voltage. The model was converted into frequency domain transfer functions that relate the stator voltage response to the field excitation voltage. As depicted in Fig. 2. 3, the basis for generator voltage control stems from the fact that there exists a low frequency region where machine voltage is dominated by a singular frequency domain model.

Two voltage sensing strategies were evaluated to extract the amplitude voltage information from the three-phase terminals of the generator, the first based on PLL methods and the second based on voltage rectification. Their frequency responses to field excitation harmonic perturbations are modeled and corroborated in Fig. 2. 5 and Fig. 2. 6 respectively. It is concluded from these results that the PLL strategy has a wider frequency region where it can be considered a valid representation of the terminal voltage response.

Excitation voltage control for regulation of the amplitude of the machine terminal voltage is realized with linear feedback control of the voltage sensed by the dqPLL. A PI compensator with high-frequency noise attenuation and hard-limiting functions was determined to be representative of the exciter system IEEE-ST1A. The time response of the control system to a sudden load increase from 0 to 250 kW is depicted in Fig. 2. 9.

# CHAPTER 3  AUTO-TRANSFORMER-RECTIFIER UNIT

This Chapter presents the design and implementation of representative thirty-pulse and eighteen-pulse auto-transformer-rectifier units (ATRU) models for simulation in Saber. Two different power ratings are desired, namely 100 kW and 20 kW. For simplicity, delta-connected auto-transformer topologies are favored to avoid the use of IPT in direct-rectification of the polyphase output. Auto-transformer design will follow the $K_g$ design approach, while winding turns have to be selected from a volt-per-turn criteria to avoid core saturation Detailed specification of wire sizes by window utilization formulas is disregarded and the wire selection criteria will be based upon current rating requirements. Basic performance test are carried in the implemented simulation models to validate the design approach.

## 3.1  Thirty-Pulse ATRU

### 3.1.1  Auto-Transformer Design

The winding diagram in Fig. 3. 1 shows a thirty-pulse auto-transformer used to derive 15 phase symmetrical output voltages from a balanced three-phase power supply. Compared to an eighteen-pulse topology, the thirty-pulse configuration might experience a decrease in reliability and efficiency due to the higher part count [15]. The topology would also increase in cost due to the added complexity in winding interconnections. The main advantage of a thirty-pulse converter is its superior input power quality, the 100 kW application will use this converter topology.

The voltage transformation ratio is obtained from the dc output voltage requirements, in this case $V_o = 540$ in the relation

$$V_o = 2\sqrt{2}\,V_{RMS}\left[\frac{N}{\pi}\sin(\pi/N)\right], \tag{1}$$

25

| Turns Ratio Phase Shift ($V_1$: $V_2$) 24° | |
| --- | --- |
| $V_a/V_1$ | 1.22 |
| $n_1/n_0$ | 0.406 |
| $n_2/n_0$ | 1.45 |
| $n_3/n_0$ | 1.15 |
| $n_4/n_0$ | 2.24 |
| $n_5/n_0$ | 3.93 |
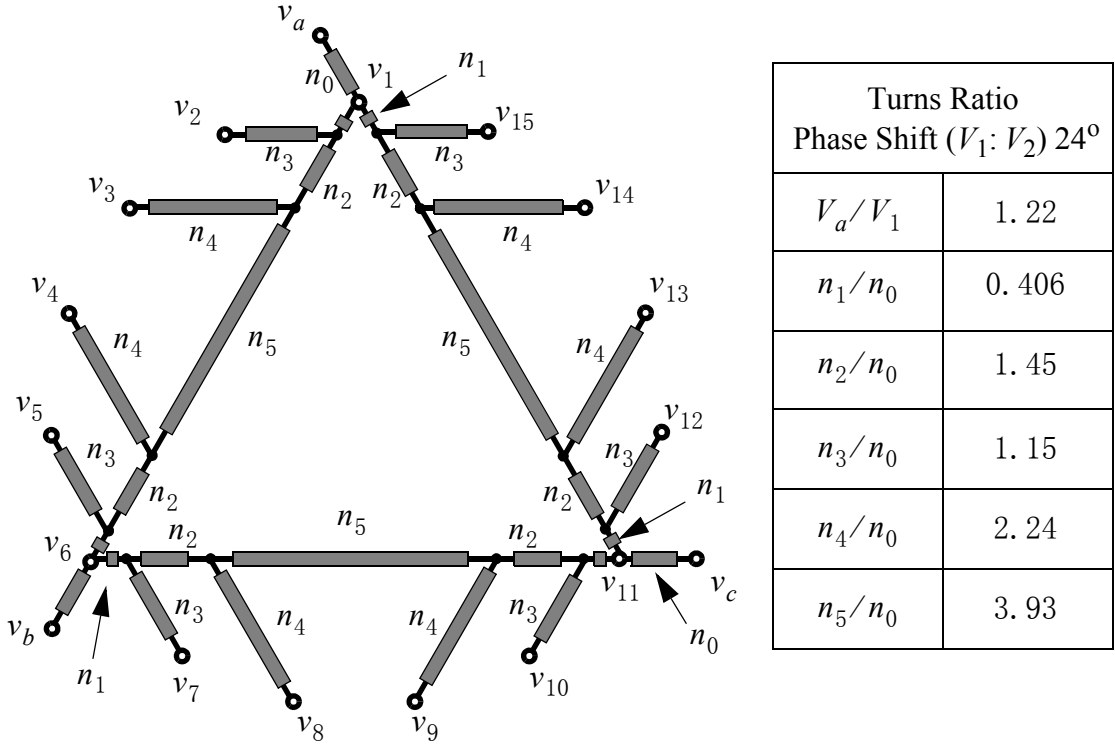
**Fig. 3. 1.** Winding diagram of symmetrical thirty-pulse auto-transformer with turns-ratio.

with $N = 15$ gives $V_{RMS} = 192$, then the ratio $V_a/V_1$ is 1.22: 1. The turns ratio of the rest of the windings are determined geometrically to have symmetric fifteen-phase output voltages.

Detailed steps in transformer design procedure can be found in [16] and [17]. The latter is of particular interest for this Thesis since it has been especially written for aerospace applications, a representative example of future energy systems with deep penetration of power electronics converters. From the scope of this Thesis, the auto-transformer design approach will focus on the major characteristics of the core such as area, length, window size and winding turns to have a reasonable design that avoids saturation of the core. More specific design details such as the bare wire area computation for winding allocation will be neglected and assumed equal for all windings.

A basic step in transformer design is the selection of the core material. In detailed designs for a given frequency range, the selection follows a trade-off of weight and cost. For the representative design scenario at hand, selection of the core is based solely on the applicable frequency range of the material. For low and medium frequencies observed in electric power systems, a commonly used material is the silicon M6X for which the flux density is 1.4 Tesla ($B = 1.4$) as listed in Table 7-1 of [17].

Once a magnetic material has been selected, the overall approach requires to compute the core size based on the power handling ability that the transformer must have for a given application. This power handling ability is represented by $K_g$, the geometric constant of the core. In order to compute the required geometric constant, the specific application at hand has the requirements listed in Table 3. 1.

**Table 3. 1. Core design requirements of 30-pulse ATRU**

| Requirement | Symbol | Value | Unit |
|---|---|---|---|
| Output power | $P_o$ | 100 | kW |
| Frequency | $f$ | 400 | Hz |
| Flux Density | $B$ | 1.4 | T |
| Regulation | $\alpha$ | 5 | % |
| Efficiency | $\eta$ | 0.95 | pu |

The core geometry is computed from [17]

$$K_g = \frac{P_t}{2(2.86 f^2 B^2 10^{-4})\alpha}, \tag{2}$$

where $P_t$ is the apparent power the transformer is designed to handle, which is equivalent to sum of input power and the load power, then

$$P_t = P_o\left(\frac{1.05}{\eta} + 1\right). \tag{3}$$

Taking the requirements of Table 3. 1, the required core geometry is $K_g = 240 \text{ cm}^5$.

The core size is selected to have the minimum requirements of power handling ability computed above, represented by $K_g$. It is clear this ability is a function of the geometric characteristics of the core, namely window size ($W_a$), core cross-sectional area ($A_c$), window utilization factor ($K_u$) and the mean length of turn ($MLT$). Table 3-11 in [17] list this characteristics for three-phase EI laminations. The required core from that table is 1800EI, with the relevant design data listed in Table 3. 2.

**Table 3. 2. Design data of core number 875 EI - 3P (from table 3.11 in [17])**

| Characteristic | Value | Unit |
|:---:|:---:|:---:|
| Weight | 12 | kg |
| MLT | 26.3 | cm |
| $A_c$ | 19.8 | cm$^2$ |
| $W_a$ | 52.3 | cm$^2$ |
| $K_g$ | 470 | cm$^5$ |
| Length | 20.54 | cm |

The specific number of primary turns is selected from a volt-per-turn criteria [17]

$$N_0 = \frac{(V_A - V_1)_{RMS}}{4.44B(A_c)f}10^4,$$ (4)

since $B = 1.4$ T, $f = 400$ Hz and $(V_A - V_1)_{RMS} = 43$ V$_{RMS}$ then $N_0 = 10$.

A detailed design approach requires to determine the window size allocated to each one of the windings in the computation of the bare wire area. In this representative design scenario, the wire size is selected from the winding ampere rating. It is reasonable to assume the wire size to be #3 AWG with an ampere capacity of 158 A$_{RMS}$. From Table 4-9 in [17], it is possible to approximate the resistance of the wire per unit length as 6.46 $\mu\Omega$/cm.

The winding resistance can now be computed from [17]

$$R_p = MLT(N_p)\left(\frac{\mu\Omega}{cm}\right)(10^{-6}),$$ (5)

and using the core data in Table 3. 2, $R_P = 1.7$ mΩ. For simplicity it will be assumed the rest of the windings use the same wire size so that ratios of resistance follow the same ratios of the winding turns.

## 3.1.2  Saber Implementation

The auto-transformer design obtained in the previous section is now implemented in Saber. Fig. 3. 2 shows the schematic of the thirty-pulse autotransformer with direct rectification of the output. Small leakage reactances are added in the output of the auto-transformer. The dc output of the converter does not require the implementation of an IPT.
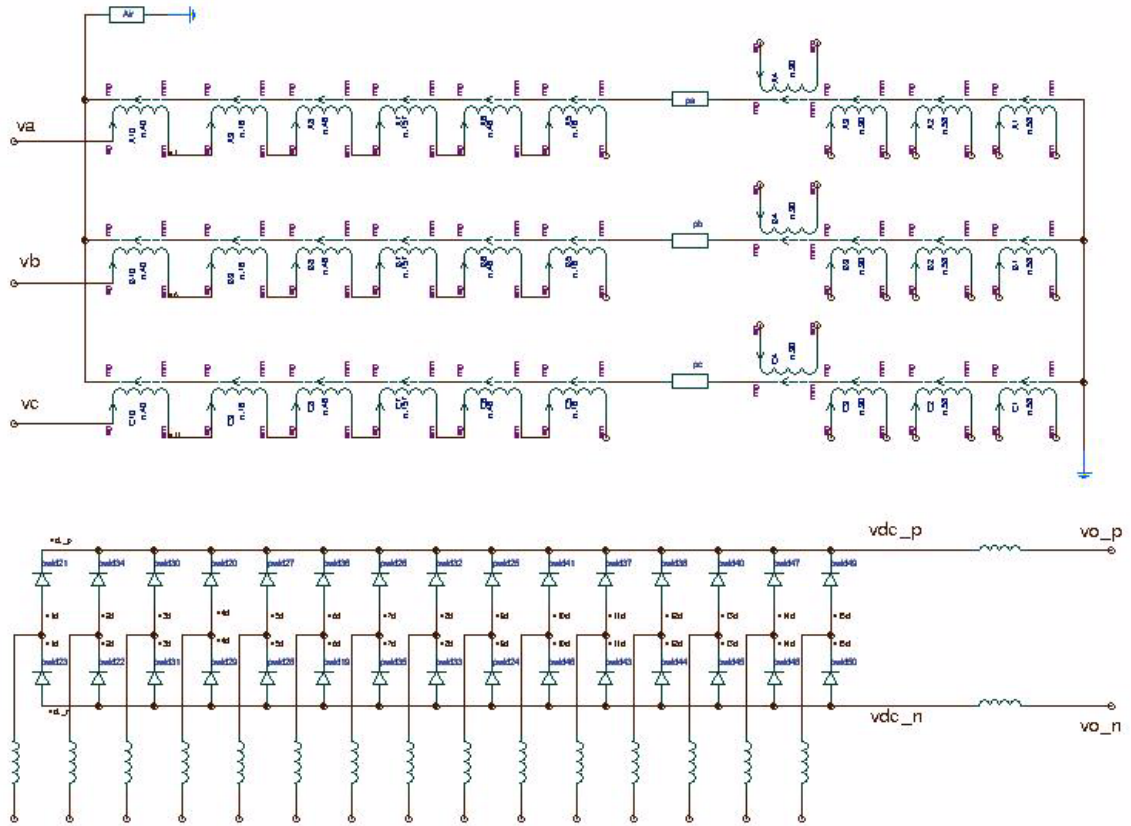


**Fig. 3. 2.** Schematic of thirty-pulse ATRU.

The parameters specifying the circuit implementation are listed in Table 3. 3. The winding resistances follow the same ratio of the turns, and only the value for $n_0$ is listed

**Table 3. 3. Parameters for 100 kW, thirty-pulse ATRU**

| Parameter | Value | Unit |
|-----------|-------|------|
| $n_0$ | 10 | turn |
| $n_1$ | 4 | turn |
| $n_2$ | 15 | turn |
| $n_3$ | 12 | turn |
| $n_4$ | 23 | turn |
| $n_5$ | 40 | turn |
| $r_{w,n0}$ | 0.0017 | mΩ |
| core length | 20.5 | cm |
| core area | 19.8 | $cm^2$ |
| relative permeability | 5000 | - |
| $L_{k1}$ | 1 | μH |

The time domain response of the dc bus voltage of the circuit is presented in Fig. 3. 3. It is clear the output contains the characteristic thirty-pulse ripple.
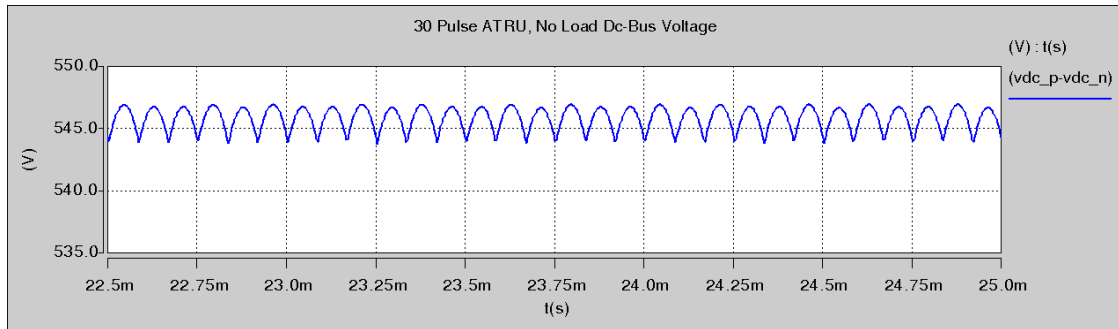


**Fig. 3. 3.** Time domain response of dc bus voltage in thirty-pulse ATRU

## 3.2  Eighteen-Pulse, T-Delta ATRU

### 3.2.1  Auto-transformer Design

Another common auto-transformer topology is the eighteen-pulse T-Delta [18]. Fig. 3. 4 shows the winding diagram and turns ratio to derive nine-phase symmetrical output voltages from a balanced three-phase supply.



| Turns Ratio Phase Shift ($v_1$: $v_2$) 40° | |
|---|---|
| $V_a/V_1$ | 1. 2 |
| $n_1/n_0$ | 1. 88 |
| $n_2/n_0$ | 6. 41 |
| $n_3/n_0$ | 0. 8 |
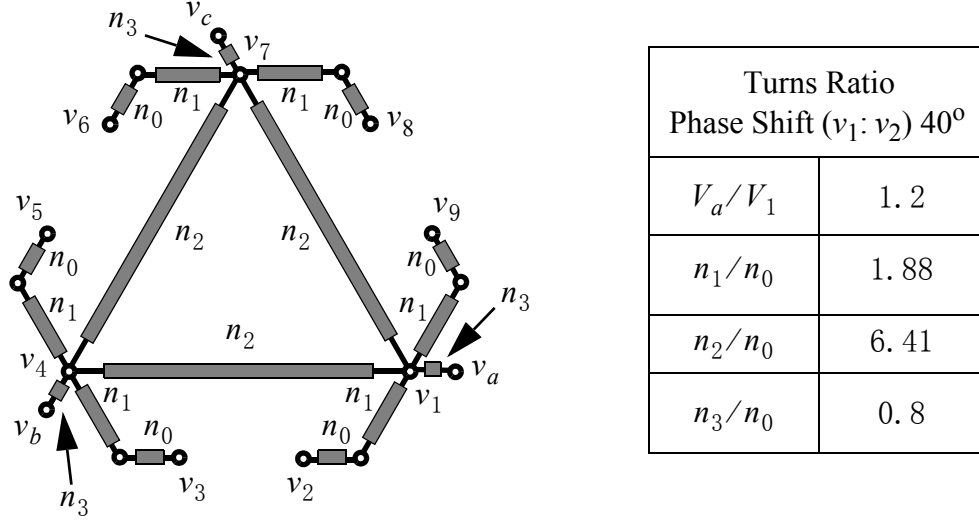
**Fig. 3. 4.**  Winding diagram of a nine-phase auto-transformer with turns-ratio.

The voltage transformation ratio is obtained from the dc output voltage requirements, in this case $V_o = 540$ in the relation

$$V_o = 2\sqrt{2}\,V_{RMS}\left[\frac{N}{\pi}\sin(\pi/N)\right],$$  (6)

with $N = 9$ gives $V_{RMS} = 195$, then the ratio $V_a/V_1$ is 1.2: 1. The turns ratio of the rest of the windings are determined geometrically to have symmetric nine-phase output voltages.

As in the thirty-pulse ATRU case, the scope is to design a representative auto-transformer design. For a detailed step-by-step procedure reference [17] is a very good source

of information in aerospace converter applications. The core material is also based on silicon M6X with $B = 1.4$ T.

The next step in the design process, is to compute core size based on the power handling ability. The specific application at hand has the requirements listed in Table 3. 4.

**Table 3. 4. Core design requirements of 18-pulse ATRU**

| Requirement | Symbol | Value | Unit |
|---|---|---|---|
| Output power | $P_o$ | 20 | kW |
| Frequency | $f$ | 400 | Hz |
| Flux Density | $B$ | 1.4 | T |
| Regulation | $\alpha$ | 5 | % |
| Efficiency | $\eta$ | 0.95 | pu |

The core geometry computed from (2) gives $K_g = 48$ cm$^5$. From Table 3-11 in [17] the required EI laminations are those corresponding to 1200EI, with the relevant design data listed in Table 3. 5.

**Table 3. 5. Design data of core number 1200EI - 3P (from table 3.11 in [17])**

| Characteristic | Value | Unit |
|---|---|---|
| Weight | 3.5 | kg |
| $MLT$ | 17.6 | cm |
| $A_c$ | 8.83 | cm$^2$ |
| $W_a$ | 23.2 | cm$^2$ |
| $K_g$ | 61.7 | cm$^5$ |
| Length | 13.6 | cm |

The specific number of primary turns is selected from the volt-per-turn criteria in (4) giving $N_3 = 19$. Since the circulating current in this winding is 166 $A_{RMS}$, it is reasonable to assume the wire used is #2 AWG with an ampere capacity of 181 A. The approximate resistance of the wire per unit length is 5.13 $\mu\Omega$/cm.

The winding resistance is computed from (5), and using the core data in Table 3. 5, $R_P = 1.7$ mΩ. For simplicity it will be assumed the rest of the windings use the same wire size so that ratios of resistance follow the same ratios of the winding turns.

## 3.2.2  Saber Implementation

Fig. 3. 5 shows the schematic of the eighteen-pulse autotransformer with direct rectification of the output. Again the dc output of the converter does not require the implementation of an IPT.
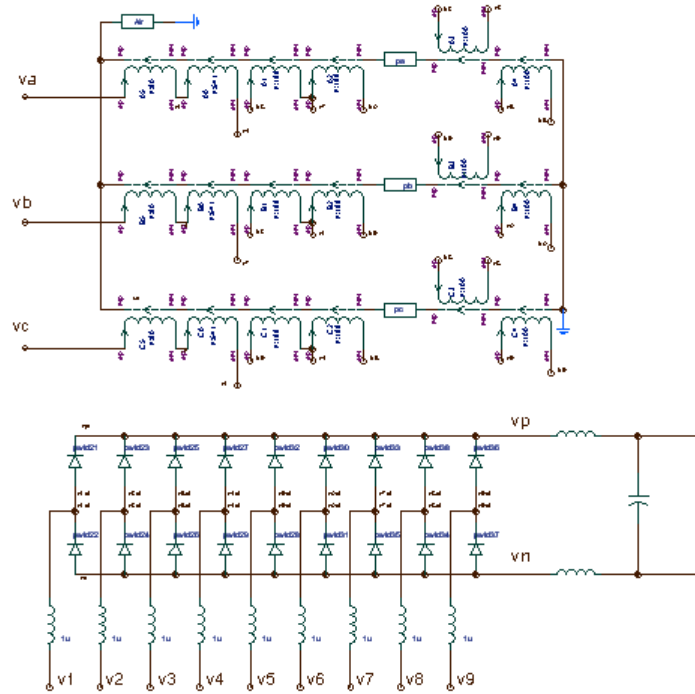


**Fig. 3. 5.**  Schematic of eighteen-pulse ATRU.

The parameters specifying the circuit implementation are listed in Table 3. 6. The winding resistances follow the same ratio of the turns, and only the value for $n_0$ is listed.

**Table 3. 6. Parameters for 20 kW, 18-Pulse ATRU**

| Parameter | Value | Unit |
|---|---|---|
| $n_0$ | 24 | turn |
| $n_1$ | 45 | turn |
| $n_2$ | 154 | turn |
| $n_3$ | 19 | turn |
| $r_{w,n0}$ | 0.0017 | mΩ |
| core length | 13.6 | cm |
| core area | 8.83 | $cm^2$ |
| relative permeability | 5000 | - |
| $L_{k1}$ | 1 | μH |

The eighteen-pulse ATRU simulation model has been widely used in simulations with the generator template, and has served as the basis for studying and demonstrating the stabilization of constant-power loads by means of passive damping techniques. The final calibration for this system required a density setting of 2 and truncation error of 0.5 μ to observe the waveform in Fig. 3. 6.
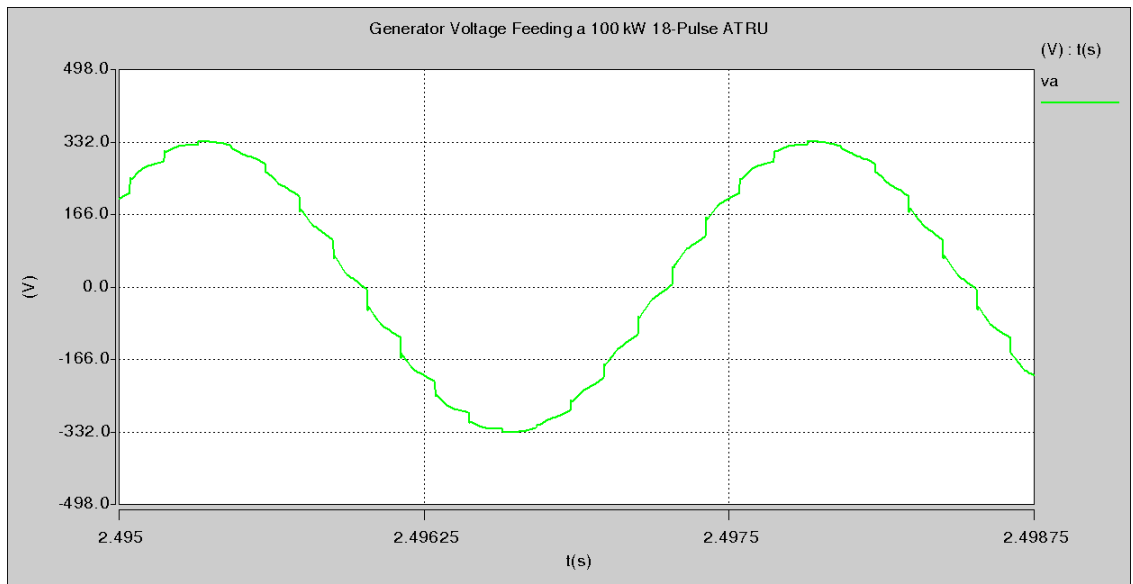
**Fig. 3. 6.** Time domain response of phase a generator voltage with 18-pulse ATRU loaded with 100 kW resistor.

## 3.3  Conclusions

This chapter has presented the design and implementation of representative thirty-pulse and eighteen-pulse ATRU models for simulation in Saber. The power ratings were given different values, the 18-Pulse converter was designed for 20 kW applications while the 30-pulse was designed to handle 100 kW. The Saber models include the switching action of the line-commutated diodes at the polyphase output of the auto-transformer. Direct rectification for delta-connected windings did not require the implementation of and IPT.

The design approach is essentially the same for both converters. Both auto-transformers were designed for the same core material, Silicon M6X. The core size is selected from the power handling ability each application requires. This power handling ability is represented by the core geometry $K_g$. From core design data, the core dimensions were selected to slightly exceed the requirement on $K_g$. Then the winding turns are selected from a volt-per-turn criteria to avoid core saturation. The wire sizes are approximated from their ampere capacity ratings. The more detailed design approach that specifies the wire gauge from the analysis of available winding area has been disregarded. The winding resistances however, are computed from the exact data corresponding to the selected core geometry.

Basic performance tests show the models are reliable representations for system simulations. In particular, the eighteen-pulse ATRU model has been widely used in simulations with the generator template.

# CHAPTER 4  VOLTAGE-SOURCED CONVERTER

This Chapter presents the switching and averaged modeling of the two-level pulse-width modulated voltage-source converter (VSC). The discontinuous time model of the converter is presented first and averaging theory is applied subsequently to obtain a continuos time model. Conventional linearization techniques are applied to the averaged model in the dq-coordinate frame for control purposes only. Converter parameters and controller settings are then given for a representative 50 kW converter model. Finally, switching and averaged models are implemented in Saber and a set of relevant tests are conducted to evaluate the correlation of the models at large signal perturbations and steady-state equilibrium points.

## 4.1  Converter Modeling

Fig. 4. 1 shows the circuit diagram of a 2-level, three-phase VSC. The source supply is identified with $v_{x,s}$ where $x = a, b, c$. The input currents $i_{x,s}$ in the boost inductors follow a rectifier convention and are defined positive as going into the converter terminals, identified with $v_{x,c}$. The switching signals are $s_{x0}$ and $s_{x1}$ for the upper and lower phase-leg switches. The positive and negative rail voltages of the dc bus are identified as $v_{dc,p}$ and $v_{dc,n}$ respectively, where the output capacitor holds the voltage to a fairly constant value.

The boost inductor dynamics are given by

$$L\frac{\mathrm{d}}{\mathrm{d}t}\begin{bmatrix} i_{a,s} \\ i_{b,s} \\ i_{c,s} \end{bmatrix} = \begin{bmatrix} v_{a,s} \\ v_{b,s} \\ v_{c,s} \end{bmatrix} - \begin{bmatrix} v_{a,c} \\ v_{b,c} \\ v_{c,c} \end{bmatrix}, \tag{1}$$

where all voltages are referenced to the supply neutral. Using the switching function definition $s_{x0}$ being 1 for the ON state and 0 for the OFF state of the upper switches, the converter voltage can be expressed as follows
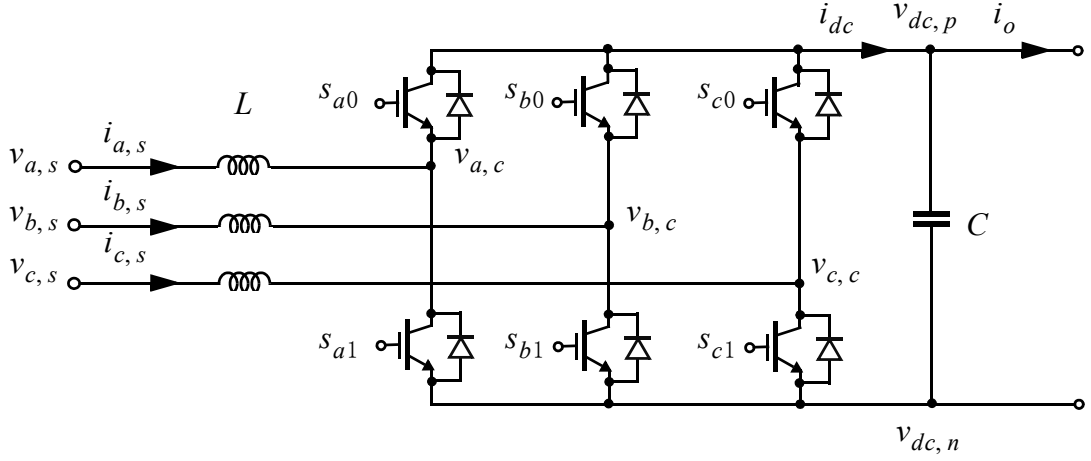
**Fig. 4. 1.** Circuit diagram of three-phase voltage-sourced converter

$$
\begin{bmatrix} v_{a,c} \\ v_{b,c} \\ v_{c,c} \end{bmatrix} = v_{dc,p} \begin{bmatrix} s_{a0} \\ s_{b0} \\ s_{c0} \end{bmatrix} + v_{dc,n} \begin{bmatrix} 1 - s_{a0} \\ 1 - s_{b0} \\ 1 - s_{c0} \end{bmatrix} = v_{dc} \begin{bmatrix} s_{a0} \\ s_{b0} \\ s_{c0} \end{bmatrix} + \begin{bmatrix} v_{dc,n} \\ v_{dc,n} \\ v_{dc,n} \end{bmatrix}, \tag{2}
$$

where it is clear $v_{dc} = v_{dc,p} - v_{dc,n}$, and the switched model of the inductor voltage is

$$
L \frac{d}{dt} \begin{bmatrix} i_{a,s} \\ i_{b,s} \\ i_{c,s} \end{bmatrix} = \begin{bmatrix} v_{a,s} \\ v_{b,s} \\ v_{c,s} \end{bmatrix} - v_{dc} \begin{bmatrix} s_{a0} \\ s_{b0} \\ s_{c0} \end{bmatrix} - \begin{bmatrix} v_{dc,n} \\ v_{dc,n} \\ v_{dc,n} \end{bmatrix}. \tag{3}
$$

The averaging method used to remove the switch discontinuity in (3) consists in assuming a very high switching frequency [3]. Defining $d_x$ as the average switch ON time duty cycle, the switching-cycle averaged model of the inductor dynamics is obtained as follows

$$
L \frac{d}{dt} \begin{bmatrix} \bar{i}_{a,s} \\ \bar{i}_{b,s} \\ \bar{i}_{c,s} \end{bmatrix} = \begin{bmatrix} \bar{v}_{a,s} \\ \bar{v}_{b,s} \\ \bar{v}_{c,s} \end{bmatrix} - \bar{v}_{dc} \begin{bmatrix} d_a \\ d_b \\ d_c \end{bmatrix} - \begin{bmatrix} \bar{v}_{dc,n} \\ \bar{v}_{dc,n} \\ \bar{v}_{dc,n} \end{bmatrix}, \tag{4}
$$

where an additional definition for balanced ($v_{a,s} + v_{b,s} + v_{c,s} = 0$), three-wire systems ($i_{a,s} + i_{b,s} + i_{c,s} = 0$) is introduced

38

$$\bar{v}_{dc,n} = -\frac{\bar{v}_{dc}}{3}(d_a + d_b + d_c).\tag{5}$$

The averaged converter model is nonlinear because of the product of the control variable $d_x$ and the state variable $\bar{v}_{dc}$, and there is not a steady-state operating point since in abc-coordinates the operating point varies sinusoidally. For control purposes, direct linearization is not possible and an alternative modeling approach shall be followed. For model simulation purposes, both the switching model of (3) and the averaged model of (4) do not have impediments for direct Saber implementation since the simulator is able to handle the nonlinearity in both of them.

The modulator model for a triangular carrier is simply

$$\begin{bmatrix} d_a \\ d_b \\ d_c \end{bmatrix} = \frac{1}{2V_{tr}} \begin{bmatrix} \bar{v}_{a,ctrl} \\ \bar{v}_{b,ctrl} \\ \bar{v}_{c,ctrl} \end{bmatrix}\tag{6}$$

where $V_{tr}$ is the amplitude of the triangular carrier in the modulator, $v_{x,ctrl}$ is the average control voltage that commands the converter voltage, and it is assumed the carrier (switching) frequency is much larger than that of the control voltage.

The dc bus capacitor dynamics are described by

$$C\frac{dv_{dc}}{dt} = i_{dc} - i_o\tag{7}$$

where $i_{dc}$ is the converter bridge output current and $i_o$ is the load current. Note the converter bridge output current satisfies the relation

$$i_{dc} = d_a i_{a,s} + d_b i_{b,s} + d_c i_{c,s}.\tag{8}$$

## 4.2   Linearization of the Converter Model

A set of dq-coordinates that rotate synchronously with the source voltage has the ability to transform the positive sequence dynamics of the converter into dc quantities, effec-

tively yielding an averaged model amenable for linearization. The need for a linear-time-invariant model derives from the objective of controlling the PWM converter. Transformation of the averaged converter model in (4) into dq-coordinates gives

$$L\frac{\mathrm{d}}{\mathrm{d}t}\begin{bmatrix} \bar{i}_{d,s} \\ \bar{i}_{q,s} \end{bmatrix} = \begin{bmatrix} \bar{v}_{d,s} \\ \bar{v}_{q,s} \end{bmatrix} - \bar{v}_{dc}\begin{bmatrix} d_d \\ d_q \end{bmatrix} - \begin{bmatrix} 0 & -L\omega \\ L\omega & 0 \end{bmatrix}\begin{bmatrix} \bar{i}_{d,s} \\ \bar{i}_{q,s} \end{bmatrix}, \tag{9}$$

where the 0-coordinate equation is dropped because balanced-operation is assumed, and $\omega$ is the angular electrical frequency of the supply voltages. Note the model still involves the product of the controlled duty cycles and the dc bus voltage, but given the fact that duty cycles now have quiescent steady-state operating points, conventional small signal linearization techniques can be applied to this model.

The modulator model in dq-coordinates is also represented by the constant-gain $1/(2V_{tr})$ which combined with (9) gives

$$L\frac{\mathrm{d}}{\mathrm{d}t}\begin{bmatrix} \bar{i}_{d,s} \\ \bar{i}_{q,s} \end{bmatrix} = \begin{bmatrix} \bar{v}_{d,s} \\ \bar{v}_{q,s} \end{bmatrix} - \frac{\bar{v}_{dc}}{2V_{tr}}\begin{bmatrix} \bar{v}_{d,ctrl} \\ \bar{v}_{q,ctrl} \end{bmatrix} - \begin{bmatrix} 0 & -L\omega \\ L\omega & 0 \end{bmatrix}\begin{bmatrix} \bar{i}_{d,s} \\ \bar{i}_{q,s} \end{bmatrix}. \tag{10}$$

It is clear from this relation that in order to decouple the dynamics of the dq-coordinate currents, a feedforward compensation scheme consists in applying a control voltage of the form

$$\begin{bmatrix} v_{d,ctrl} \\ v_{q,ctrl} \end{bmatrix} = \begin{bmatrix} v_{d,ctrl}^u \\ v_{q,ctrl}^u \end{bmatrix} + \frac{2V_{tr}}{\bar{v}_{dc}}\omega L\begin{bmatrix} i_{q,ref} \\ -i_{d,ref} \end{bmatrix}, \tag{11}$$

such that, if the converter current can track the commanded reference, the control dynamics shall be decoupled.

Another possible linearization approach simplifies significantly the converter model, and consists in assuming the dc voltage dynamics are much slower than the inductor current dynamics such that $\bar{v}_{dc}$ can be considered constant in the current control loop. The

model in (9)-(11) becomes linear and conventional control system frequency domain analysis is possible.

The linear, time-invariant inductor current model has the transfer functions

$$
\begin{aligned}
I_{d,s}(s) &= \frac{T_i(s)}{1 + T_i(s)} I_{d,ref}(s) + \frac{1/(sL)}{1 + T_i(s)} V_{d,s}(s) - \frac{\omega/s}{[1 + T_i(s)]^2} I_{q,ref}(s) \\
I_{q,s}(s) &= \frac{T_i(s)}{1 + T_i(s)} I_{q,ref}(s) + \frac{1/(sL)}{1 + T_i(s)} V_{q,s}(s) + \frac{\omega/s}{[1 + T_i(s)]^2} I_{d,ref}(s)
\end{aligned}
\tag{12}
$$

where the open-loop current control gain was introduced and is defined as

$$
T_i(s) = -\frac{V_{dc}}{2V_{tr}(sL)} H_i(s).
\tag{13}
$$

The plant for current control has a pole at the origin because the resistance of the inductor has been neglected. Fig. 4. 2 shows the schematic of the current controller implemented in Saber.
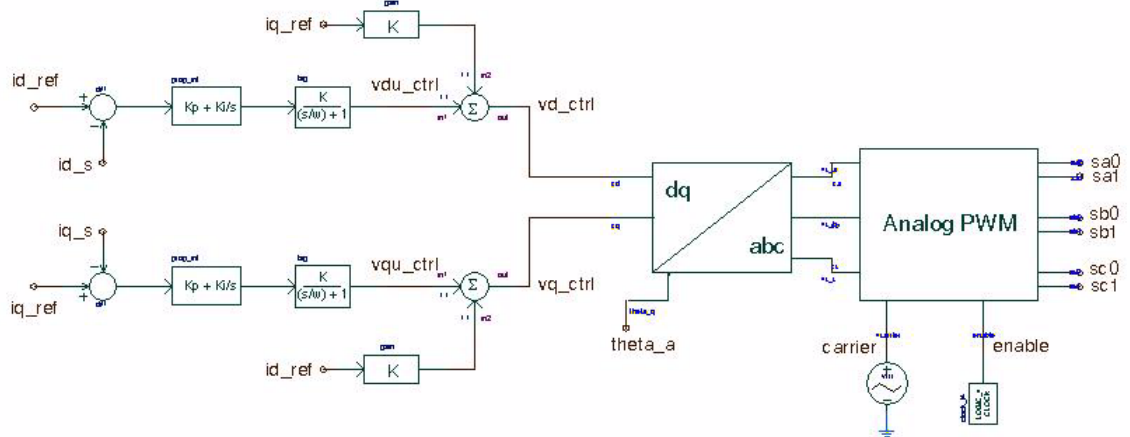


**Fig. 4. 2.** Schematic of dq-coordinate controller and pulse-width modulator for switching model of the three-phase VSC.

The slower voltage control loop requires the use of the power balance equation in dq-coordinates

$$v_{dc}i_{dc} = v_{d,s}i_{d,s} + v_{q,s}i_{q,s} + v_{0,s}i_{0,s}, \tag{14}$$

where $v_{q,s} = 0$ because the dq-coordinate frame is aligned with the source voltage. Simplifying and introducing the result in (7) gives a nonlinear model of the output voltage

$$C\frac{dv_{dc}}{dt} = \frac{v_{d,s}i_{d,s}}{v_{dc}} - i_o, \tag{15}$$

but again the model can be linearized for small-signal deviations from a quiescent operating point.

Assuming a purely resistive load $i_o = v_{dc}/R$ and using the d-axis current expression in (12) with the linearized capacitor voltage model of (15) gives the transfer function

$$V_{dc}(s) = \frac{K_{dc}}{1+s/\omega_{dc}} \cdot \frac{T_i(s)}{1+T_i(s)} I_{d,ref}(s), \tag{16}$$

where

$$K_{dc} = \frac{V_{d,s}}{\dfrac{V_{d,s}I_{d,s}}{V_{dc}} + \dfrac{V_{dc}}{R}}, \tag{17}$$

and

$$\omega_{dc} = \left(\frac{V_{d,s}I_{d,s}}{V_{dc}^2} + \frac{1}{R}\right)/C. \tag{18}$$

Note the resistive load changes both the gain and pole location of the transfer function. Moreover, under no load conditions $R \to \infty$ and $I_{d,s} = 0$, so that the plant would have a pole at the origin.

The voltage controller open-loop gain is then given by

$$T_v(s) = \frac{K_{dc}}{1+s/\omega_{dc}} \cdot \frac{T_i(s)}{1+T_i(s)} H_v(s) \quad . \tag{19}$$

The schematic in Fig. 4. 3 shows the voltage control loop commanding the reference of the d-axis current, while the q-axis current is commanded to zero for unity power factor. A limiter has been



**Fig. 4. 3.** Schematic of voltage control loop.

added to avoid loading the converter above its rated current during the start up transient of the dc bus voltage.

## 4.3 Model Parameters

The parameters for representative rectifier with input voltage of 115 $V_{RMS}$ per phase and 540 V dc-output voltage are found in Table 4. 1. The switching frequency is set to 20 kHz for a rated power of 50 kW, while the inductor and capacitor where selected based on 10% current and voltage ripples.

**Table 4. 1. Parameters for 50 kW, 115 $V_{RMS}$ (L-N) to 540 V, SPWM Rectifier**

| Parameter | Value | Unit |
|---|---|---|
| Switching $f$ | 20 | kHz |
| Boost Inductor | 100 | μH |
| Dc Bus Capacitor | 35 | μF |
| $V_{tr}$ | 1 | V |

For current control purposes, a PI compensator is sufficient for this application, ensuring good tracking of the input while providing phase margin compensation

$$H_i(s) = -\left(K_P + \frac{K_I}{s}\right)\left(\frac{1}{1 + s/\omega_p}\right). \tag{20}$$

A high-frequency pole is placed at 10 times the crossover frequency to attenuate further the switching ripple in the control loop. The proposed design with 430 Hz crossover frequency and 79 degrees of phase margin requires setting $K_P = 9.95 \cdot 10^{-4}$, $K_I = 0.25$ and $\omega_p = 2\pi \cdot 4000$. The bandwidth of the regulator is not extended to 1/10 of the

switching frequency in the event that it is required to allocate the load regulation bandwidth.

The voltage compensator is a simple PI compensator designed to have a bandwidth of approximately 14 Hz and 108 degrees of phase margin at full-load conditions, while the no load bandwidth increases to 450 Hz with a phase margin of 32 degrees. The corresponding compensator gains are $K_P = 0.2984$ and $K_I = 75$. If the converter power is doubled and the switching frequency is halved, the same inductor and current control design apply. However, the voltage regulation needs to be adjusted and so does the capacitor, which is increased to 120 μF. The voltage compensator in this case is designed for a full-load bandwidth of 36 Hz and phase margin of 128 degrees, while the no load bandwidth increases to 450 Hz with a phase margin of 32 degrees. The corresponding compensator gains are $K_P = 1.19$ and $K_I = 300$.

## 4.4   Switching Model Implementation

Fig. 4. 4 shows the circuit schematic of the Saber implementation of the switching model of the VSC. The variables names identified in the figure follows the definitions used within the Chapter. A dqPLL is included in the model for reference angle detection and dq-coordinate transformation for application of the control model revised in the previous sections.

Fig. 4. 5 shows the current regulation at the converter input. Unity power factor is achieved by commanding the q-axis current to zero. The peak to peak ripple current variation is 22.1 A, approximately 10.8% of the peak rectifier current (205 A) at rated three-phase power (50 kW).
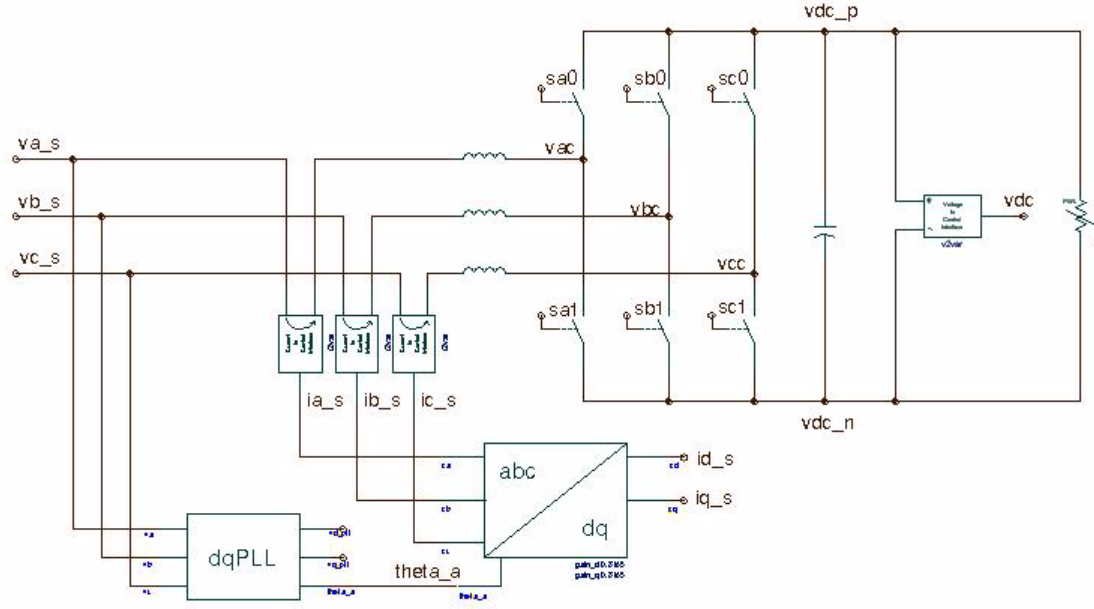
**Fig. 4. 4.** Schematic of the switching model of the three-phase VSC with dqPLL voltage sensor for abc to dq transformation.

## 4.5  Averaged Model Implementation

Fig. 4. 6 shows a simple implementation in Saber of the averaged model of the boost inductor and modulator based on (4)-(7). The power inputs are the source voltages $v_{x,s}$. The current sensors and their transformation into the dq-coordinate frame are identical to the full-order circuit. Additional inputs are the control voltages $v_{x,ctrl}$ and the dc bus voltage $v_{dc}$. The limiters in the duty-cycle signal generation saturate at $\pm 0.5$, and model the overmodulation region of the PWM. The saturation region is based on (7), if the control voltages were clamped to $\pm V_{tr}$, it is clear the duty-cycle signals would clamp to $\pm 0.5$.

The switching-cycle averaged model of the capacitor dynamics were modeled by (40) and its implementation is shown in Fig. 4. 7. The inductor currents are the state-variables that together with the control duty ratios contributed to the charging currents of the dc bus capacitor. The negative rail voltage is generated based on (5) using a linear combination of the control duty ratios multiplied by the resulting dc bus voltage.
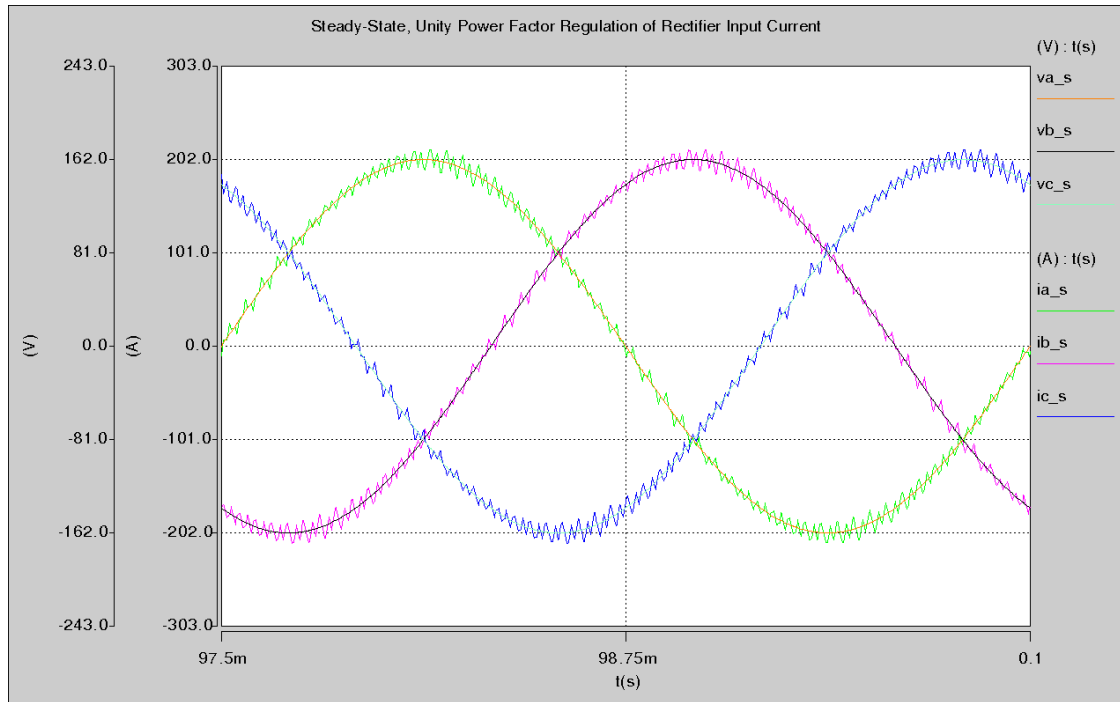
**Fig. 4. 5.** Time domain response of switching converter input current in steady-state.

## 4.6 Correlation of Switching and Averaged Models

Both switching models and averaged models use the same controller settings allowing direct comparison of model dynamics for circuit transients. Since the averaged models are large-signal models, the correlation tests need not to be limited to small perturbations. The tests performed include the start up transient of the dc bus voltage, the steady-state input current regulation and the sudden dc load removal.

The time domain response of the dc bus voltage during the start up transient of the switching and averaged models is depicted in Fig. 4. 8. Both models exhibit excellent correlation and the averaged model follows the dynamics of the switching model dynamics exactly with the exception of the small switching ripple.

The converter input current during the start up transient of the dc bus voltage is depicted in Fig. 4. 9 for both the switching and averaged models. Once again excellent
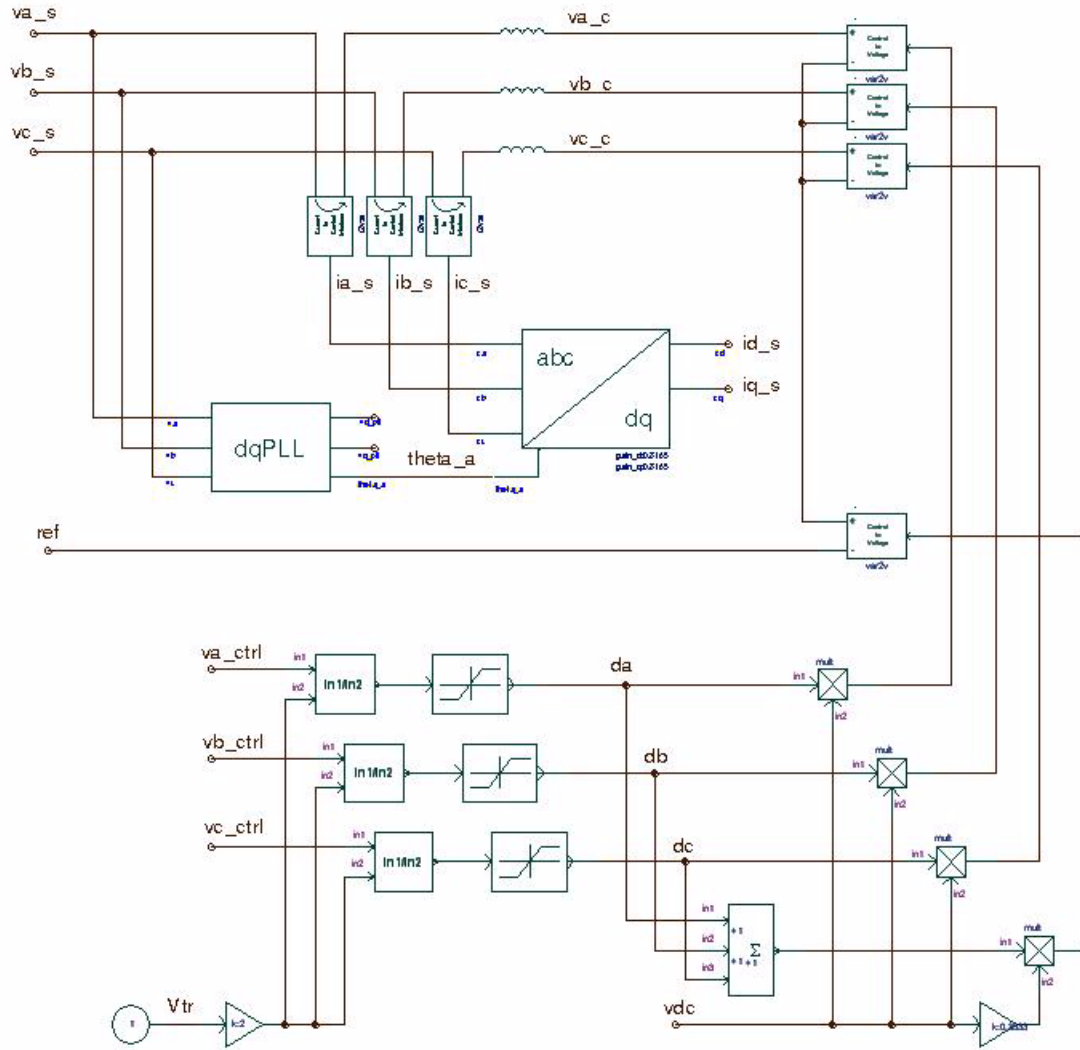
**Fig. 4. 6.** Schematic of averaged model of boost inductor voltage and modulator.

correlation of the averaged model with the switching model is observed. This test together with the one conducted for the dc bus voltage allows to conclude the averaged model is a reliable representation of the switching model during the initialization period of the PWM rectifier.
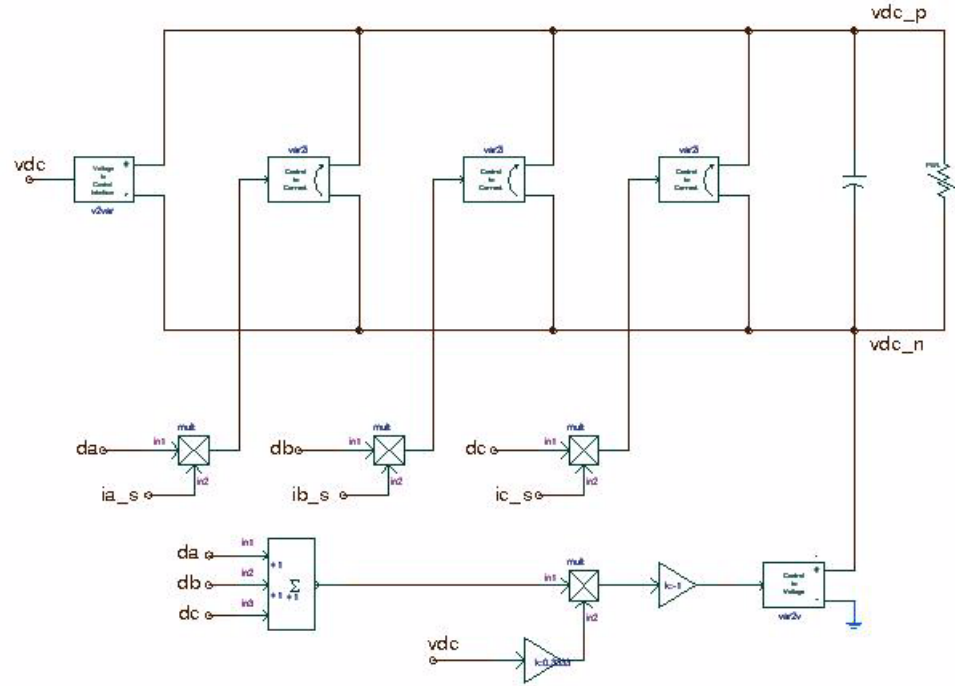
**Fig. 4. 7.** Schematic of averaged model of dc bus capacitor charging currents.
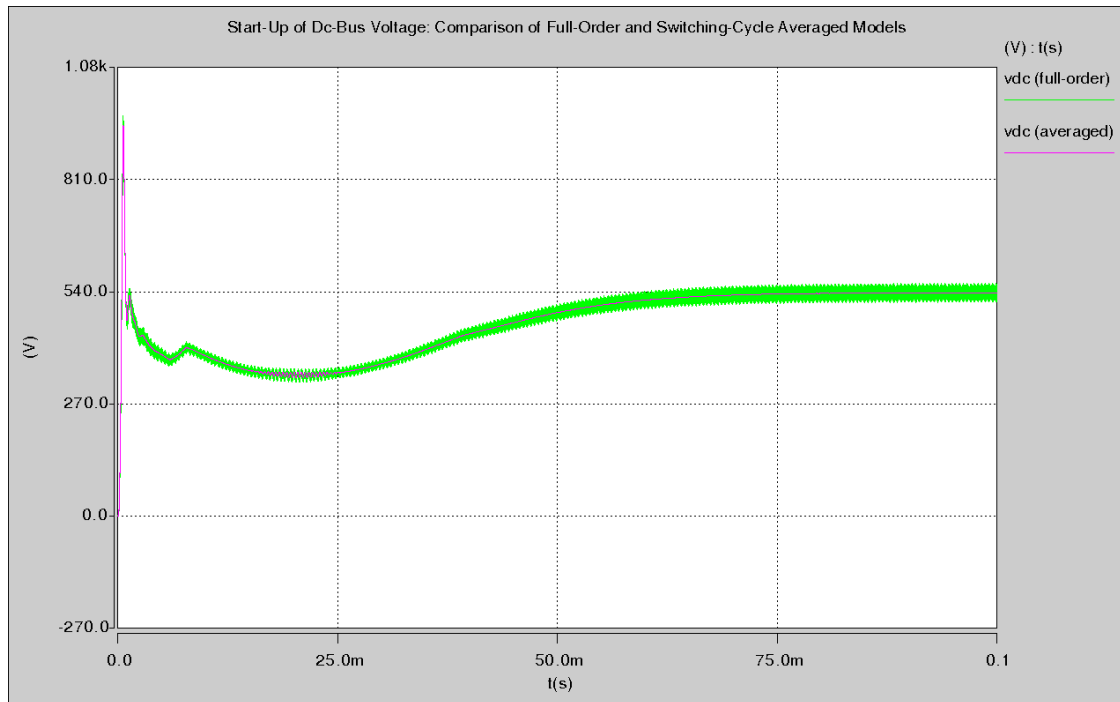


**Fig. 4. 8.** Time-domain response at start up of dc bus voltage: comparison of switching and averaged models.
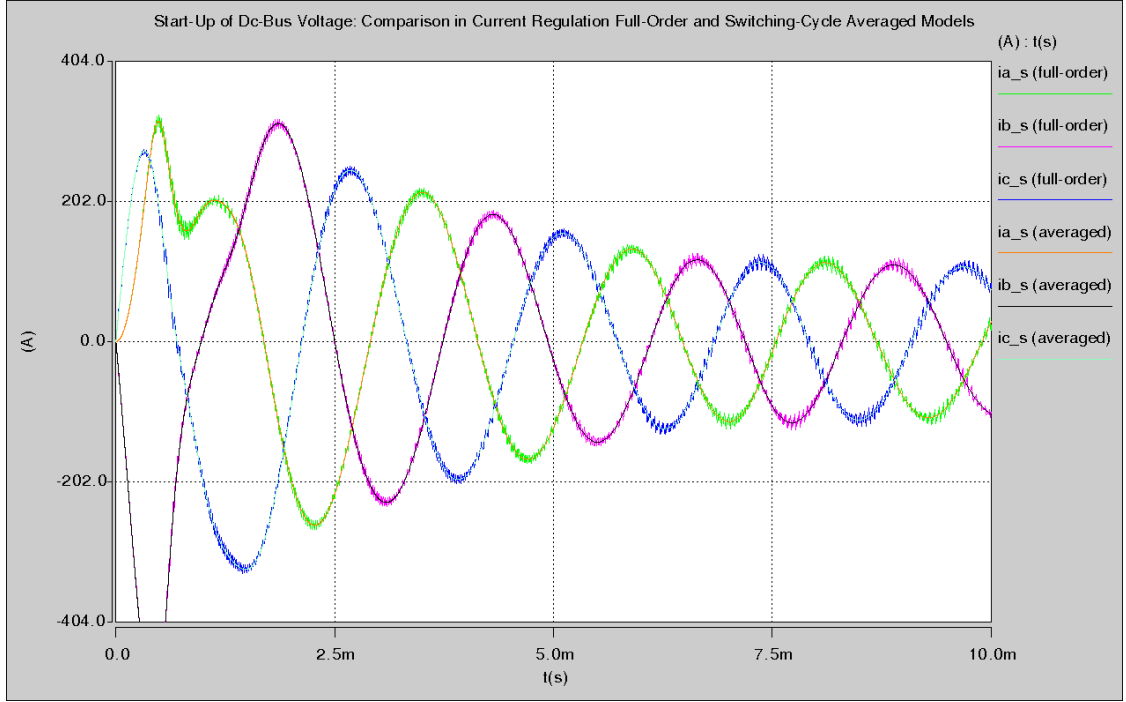
**Fig. 4. 9.** Time domain response of current regulation at start up of dc bus voltage: comparison of switching and averaged models.

Following the converter start up transient, the steady-state input current regulation of the two models is compared as depicted in Fig. 4. 10. This test proves both averaged and switching models converge to the same equilibrium point at steady-state and with full-load conditions

The final test follows the steady-state operating point and consists in a sudden removal of the dc load of the converter. Fig. 4. 11 depicts the transient response of the dc bus voltage of both switching and averaged models. The comparison proves the averaged model can also be used to accurately represent the dynamics of the switching model when the small voltage ripple is not the major subject of study.

49
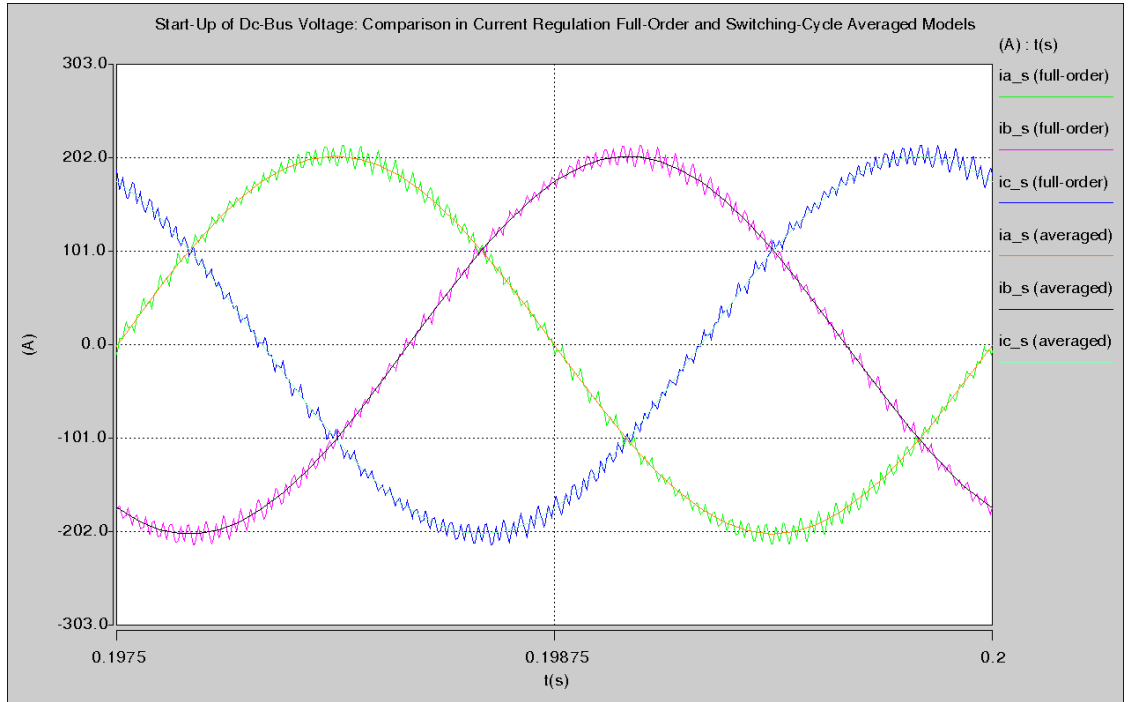
**Fig. 4. 10.** Time-domain response of current regulation at steady-state: comparison of switching and averaged models
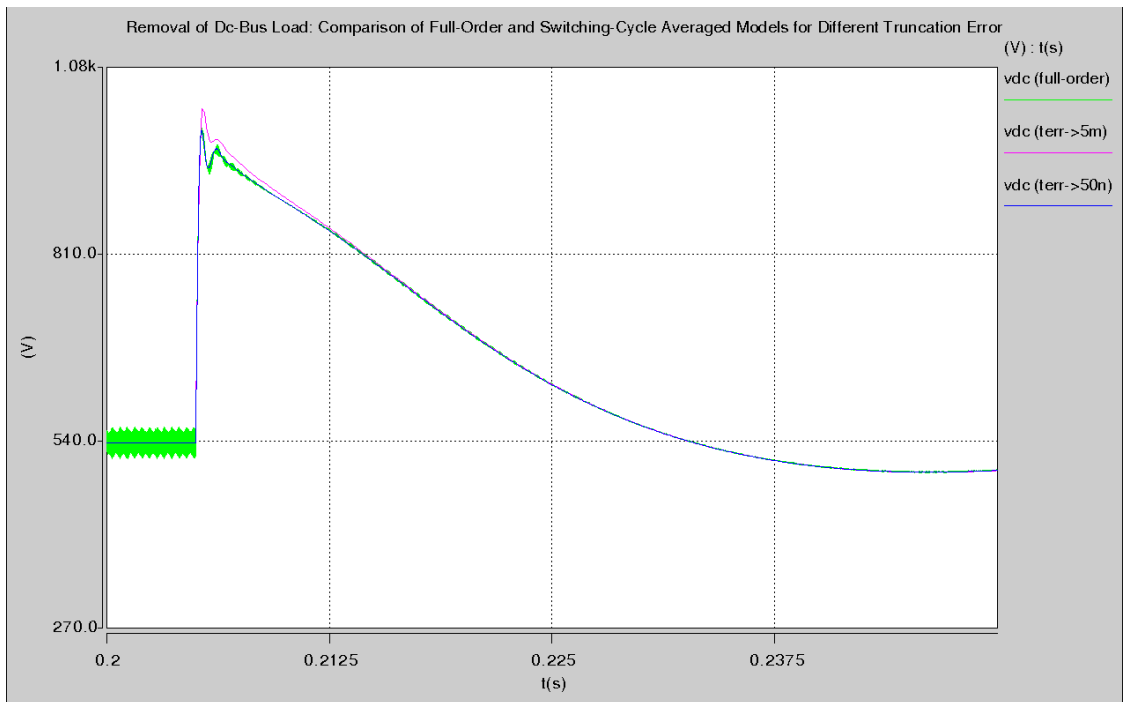


**Fig. 4. 11.** Time-domain response at removal of dc bus load: effect of changes in truncation error of averaged model

## 4.7  Conclusions

This chapter has presented the switching and averaged model development and implementation for a two-level PWM VSC. The discontinuous time model of the converter is presented first and averaging theory is applied subsequently to obtain a continuos time model. The model is still nonlinear, but modeling in an appropriate set of dq-coordinates allows to linearize the model for control purposes. Representative converter parameters and controller settings have been presented for a 50 kW converter. Simulation models are implemented for both the switching and averaged models in Saber. A series of relevant tests are conducted to evaluate the correlation of the models.

The initialization period of the converter represents involves a large inrush current for charging the dc bus capacitor. The transient dynamics of the dc bus voltage in the averaged model has proven to follow exactly the behavior of the switching model excluding the small switching ripple. In addition the input current dynamics of the averaged model have also been correlated to the those in the switching model. These two results allow to conclude the averaged model is a reliable representation of the switching model behavior during the large signal transient that represents the initialization period of the converter.

Following the initialization period, both the switching model and averaged models converge to a common steady-state equilibrium point at full load conditions. Following this quiescent condition, another large signal perturbation is introduced to the models for testing their correlation by removing the dc load. Both models experience the same large dc voltage excursion and converge to the a new common steady-state operating point at no load conditions.

There still exist limitations on the accuracy of the developed averaged model as a valid representation of the switching model. One pertaining limitation stems from averaging theory and begins at half the switching frequency of the converter. A second limitation follows from the assumption of balanced three-phase supply in the averaged converter model. Excluding this two possible scenarios and summarizing the findings of this Chap-

ter, the averaged model of the converter has proven to be a reliable representation of the switching converter during its initialization period, its steady-state equilibrium point and the large perturbation following a dc load removal.

# CHAPTER 5 VARIABLE FREQUENCY MOTOR DRIVES

This Chapter presents the modeling and control of the permanent magnet (PM) motor and wounded-rotor synchronous machine (SM) in variable speed motor drive applications. The voltage source converter (VSC) is used to command the motor terminal voltage to drive the motor at the desired speed. The modeling approach in both machines is similar, but because of the absence of damper windings in the PM motor the specific transfer functions for motor control differ. Both switching and averaged models of the VSC from Chapter 4 are implemented and evaluated to show the validity of the linearized control models and the accuracy of the averaged model to represent the dynamics of the switching models.

## 5.1 Permanent Magnet Motor Drive

### 5.1.1 Drive Modeling and Current Control

The permanent magnet synchronous machine could be conceived as a particular case of the wounded rotor type in which the field excitation current $i_{fd}$ is constant. As a result the flux linkages

$$\psi_{fd} = L_{md}I_{fd}, \tag{1}$$

are also constant when the magnetizing inductance $L_{md}$ does not vary. The modeling of the machine terminal voltage follows essentially the same procedure of that in Chapter 2. One simplification in this case is that the damper windings are not modelled in PM motors due to the relatively high electrical resistivity of the magnets and because it is common not to equip these motors physically with damper windings [27].

The stator voltage equations of the PM motor in the dq-coordinate frame are given by

$$v_d = r_s i_d - \omega_r (L_q i_q) + \frac{d}{dt}(L_d i_d + \psi_{fd})$$

$$v_q = r_s i_q + \omega_r (L_d i_d + \psi_{fd}) + \frac{d}{dt}(L_q i_q) \; , \tag{2}$$

$$v_0 = r_s i_0 + \frac{d}{dt}(L_{ls} i_0)$$

where $[v_d, v_q, v_0]$ is the motor terminal voltage, $[i_d, i_q, i_0]$ is the motor input current, $\omega_r$ is the shaft speed, $r_s$ is the stator winding resistance, $L_{ls}$ is the stator leakage inductance, and $L_d$ and $L_q$ represent the d- and q-axis synchronous inductances respectively.

Control motor speed is possible through control of the magnitude, phase and frequency of the motor current by means of a VSC. In particular, it is desirable to align the rotating stator MMF in quadrature with the pole MMF in order to achieve maximum torque per ampere control. In a dq-coordinate frame aligned with the pole axis, this control strategy is equivalent to commanding the d-axis current to zero.

It is known from Chapter 4 the VSC modulates the converter average voltage by inflicting changes in the converter duty cycle as given by the following model

$$\begin{bmatrix} \bar{v}_{a,c} \\ \bar{v}_{b,c} \\ \bar{v}_{c,c} \end{bmatrix} = \bar{v}_{dc} \cdot \begin{bmatrix} d_a \\ d_b \\ d_c \end{bmatrix} - \frac{\bar{v}_{dc}}{3} \cdot \begin{bmatrix} d_a + d_b + d_c \\ d_a + d_b + d_c \\ d_a + d_b + d_c \end{bmatrix}, \tag{3}$$

where $d_x = v_{x,ctrl}/(2V_{tr})$ with $v_{x,ctrl}$ being the control signal at the input of the modulator, $V_{tr}$ is the amplitude of the triangular carrier signal and $x$ represents each one of the three phases, namely $a$, $b$ and $c$. In the dq-coordinates of the rotor, the converter and modulator voltage model simplifies to

$$\begin{bmatrix} \bar{v}_{d,c} \\ \bar{v}_{q,c} \end{bmatrix} = \frac{\bar{v}_{dc}}{2V_{tr}} \cdot \begin{bmatrix} \bar{v}_{d,ctrl} \\ \bar{v}_{q,ctrl} \end{bmatrix}. \tag{4}$$

The motor terminals are connected directly to the converter terminals when the high-frequency switching ripple is not a concern in the drive operation, also allowing direct combination of (2) and (4). The resulting model is the essence of the motor drive since it unifies the dynamics of the VSC and the motor by establishing a relationship between control voltages and motor currents given by

$$\bar{v}_{d,ctrl} = \frac{2V_{tr}}{\bar{v}_{dc}} \cdot \left[ r_s i_d - \omega_r (L_q i_q) + \frac{d}{dt}(L_d i_d + \psi_{fd}) \right]$$
$$\bar{v}_{q,ctrl} = \frac{2V_{tr}}{\bar{v}_{dc}} \cdot \left[ r_s i_q + \omega_r (L_d i_d + \psi_{fd}) + \frac{d}{dt}(L_q i_q) \right] \tag{5}$$

The model in (5) is linear if the speed and dc voltage dynamics are assumed much slower than those of the motor currents, and they are effectively considered constant in current control. In addition, the model shows the dq-coordinate currents are coupled to each other, since the q-axis current will respond to changes in the d-axis current and vice-versa. However, a feedforward compensation technique consists in applying a control voltage of the form

$$\bar{v}_{d,ctrl} = \bar{v}_{d,ctrl}^u + \frac{2V_{tr}}{V_{dc}} L_q \cdot (-\omega_{ref}) \cdot i_{q,ref}$$
$$\bar{v}_{q,ctrl} = \bar{v}_{q,ctrl}^u + \frac{2V_{tr}}{V_{dc}} L_d \cdot (\omega_{ref}) \cdot i_{d,ref} \tag{6}$$

to almost cancel the cross-coupling terms.

For current control compensator design, the linear-time-invariant model is converted to the following frequency domain transfer functions

$$I_d(s) = \frac{T_{od}(s)}{1 + T_{od}(s)} I_{d,ref}(s) + \frac{1}{1 + T_{od}(s)} \cdot \frac{L_q}{r_s + sL_d} \cdot [\omega_r I_q(s) - \omega_{ref} I_{q,ref}(s)]$$
$$I_q(s) = \frac{T_{oq}(s)}{1 + T_{oq}(s)} I_{q,ref}(s) + \frac{1}{1 + T_{oq}(s)} \cdot \frac{-L_d}{r_s + sL_q} \cdot [\omega_r I_d(s) - \omega_{ref} I_{d,ref}(s)] \tag{7}$$

where the open-loop transfer functions were defined as

$$T_{od}(s) = \frac{V_{dc}}{2V_{tr}(r_s + sL_d)} H_{id}(s)$$

$$T_{oq}(s) = \frac{V_{dc}}{2V_{tr}(r_s + sL_q)} H_{iq}(s) \qquad (8)$$

In (7) note the decoupling function performance depends on the capability of the current control loop to follow the commanded reference. With perfect current control, $I_q(s) = I_{q,ref}(s)$ and $I_d(s) = I_{d,ref}(s)$, effectively eliminating the cross coupling.

The functional block diagram showing the current control loops is depicted in Fig. 5. 1. The feedforward terms use the commanded current references for decoupling the current control loops. As can be inferred from (6) the feedforward gains were defined as

$$K_{id}(s) = -\frac{2V_{tr}}{V_{dc}} L_q$$

$$K_{iq}(s) = \frac{2V_{tr}}{V_{dc}} L_d \qquad (9)$$

The control voltages in the output of the control stage are converted to abc-coordinates and injected as commands to the modulator of the VSC.

## 5.1.2 Speed Control

The shaft speed dynamics for the motor are given by

$$T_m = T_e - B\omega_r - J\frac{d\omega_r}{dt}, \qquad (10)$$

where $T_m$ is the mechanical torque, $T_e$ is the electromagnetic torque, $B$ and $J$ are the damping and inertial constants of the motor.

In order to control speed, a relationship has to be established between shaft speed and motor currents. The relationship is obtained through the expression for electromagnetic torque, which is obtained from a power balance equation. Assuming balanced operation, the zero axis components are dropped, and the total input power to the motor is given by
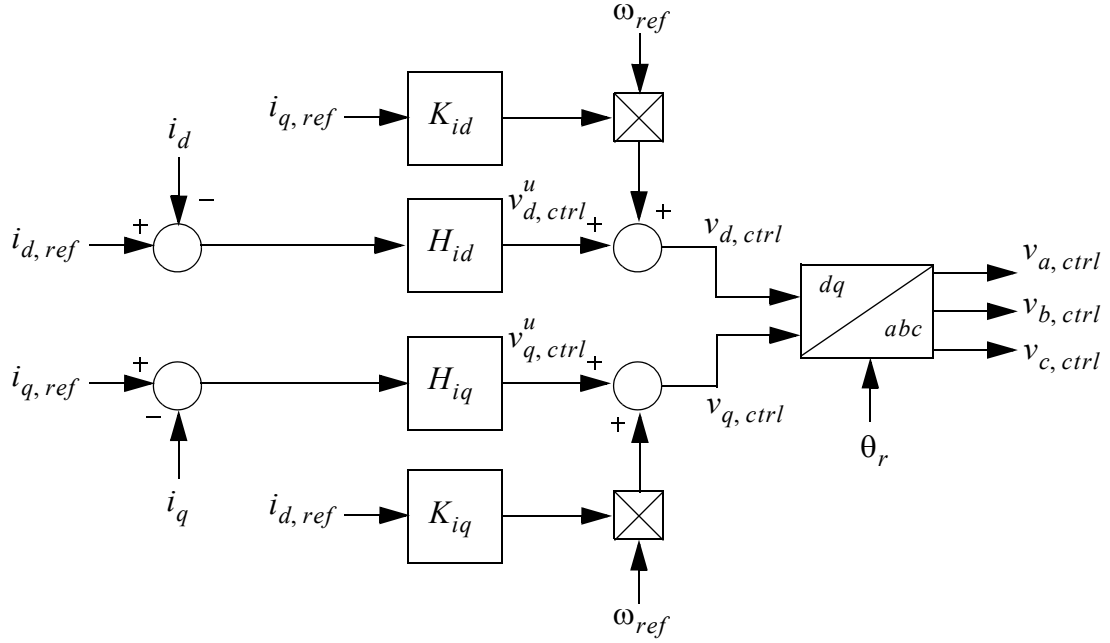
**Fig. 5. 1.** Functional block diagram of current control loop in permanent magnet motor drive.

$$P_{in} = v_d i_d + v_q i_q$$
$$= r_s i_d^2 - \omega_r L_q i_q i_d + i_d \frac{d}{dt}[L_d i_d] + r_s i_q^2 + \omega_r (L_d i_d + \psi_{fd}) i_q + i_q \frac{d}{dt}[L_q i_q] \quad . \quad (11)$$

In (11), the terms can be separated into resistive losses, inductive energy storage and speed related terms. The last set of speed related terms give the electromagnetic power transferred through the air gap of the machine, this torque is a function of the stator currents as follows

$$T_e = (L_d i_d + \psi_{fd}) i_q - L_q i_q i_d = i_q [\psi_{fd} + (L_d - L_q) i_d]. \quad (12)$$

The term $\psi_{fd} i_q$ is the torque resulting from the pole excitation, while the term $(L_d - L_q) i_d i_q$ is called the reluctance torque.

The electromagnetic torque equation in (12) is linearized with standard small-signal methods. Assuming maximum torque per ampere control, the functional block diagram for speed control is obtained as in Fig. 5. 2. Note the mutual coupling of dq-coordinate

currents is neglected since at the very low frequency range where speed control occurs, it can be assumed the motor currents follow their references perfectly.
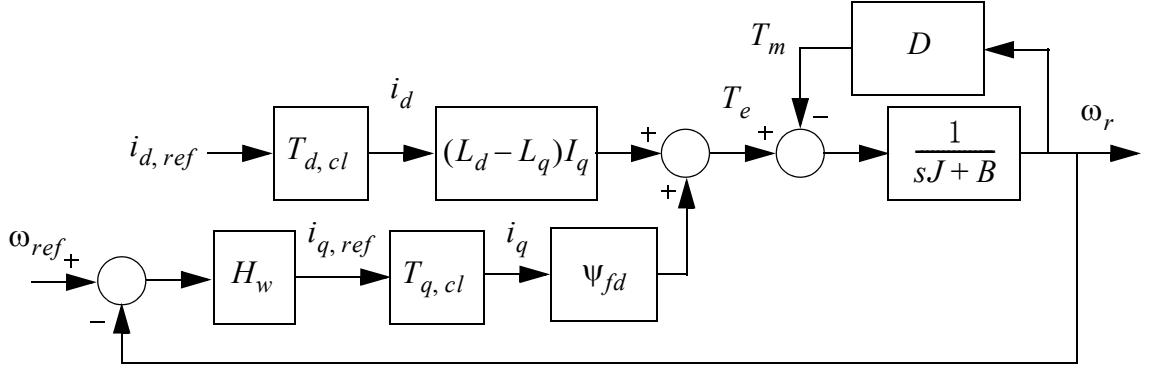


**Fig. 5. 2.** Functional block diagram of speed control loop in permanent magnet motor drive.

The open-loop transfer function for speed compensator design is

$$T_{ow}(s) = \frac{H_w(s)T_{q,cl}(s)\psi_{fd}}{sJ + (B+D)} \; ,$$  (13)

where $H_w(s)$ is the speed compensator and $T_{q,cl}(s)$ is the closed loop q-axis current control.

### 5.1.3  Saber Implementation

The schematic in Fig. 5. 3 shows the switching model of the VSC feeding the PM motor. The dc voltage supply is the source of power to the motor drive. The control inputs are the terminals identified with $v_{x,ctrl}$ going into the modulator. The abc-coordinate current signals are converted to the rotor dq-coordinate frame using the angle information extracted from direct measurement of the rotor position. The PM motor template has star-connected windings but allows to set the neutral to floating or grounded configurations. Because no unbalanced conditions are considered here, there shall be no difference in the selection. The initialization of the *dq3pmsyn* template requires to run a dc analysis first for easier convergence since the flux linkages in the rotor cannot physically have a step change from $t = 0$ to $t = 0^+$. In order to run a dc analysis the output of any PI compen-

sators in the control stage can be set to zero. If no dc-analysis can be performed, increasing the target iterations to 48 and the maximum iterations to 800 has shown the same results as with the case where there is a dc analysis.
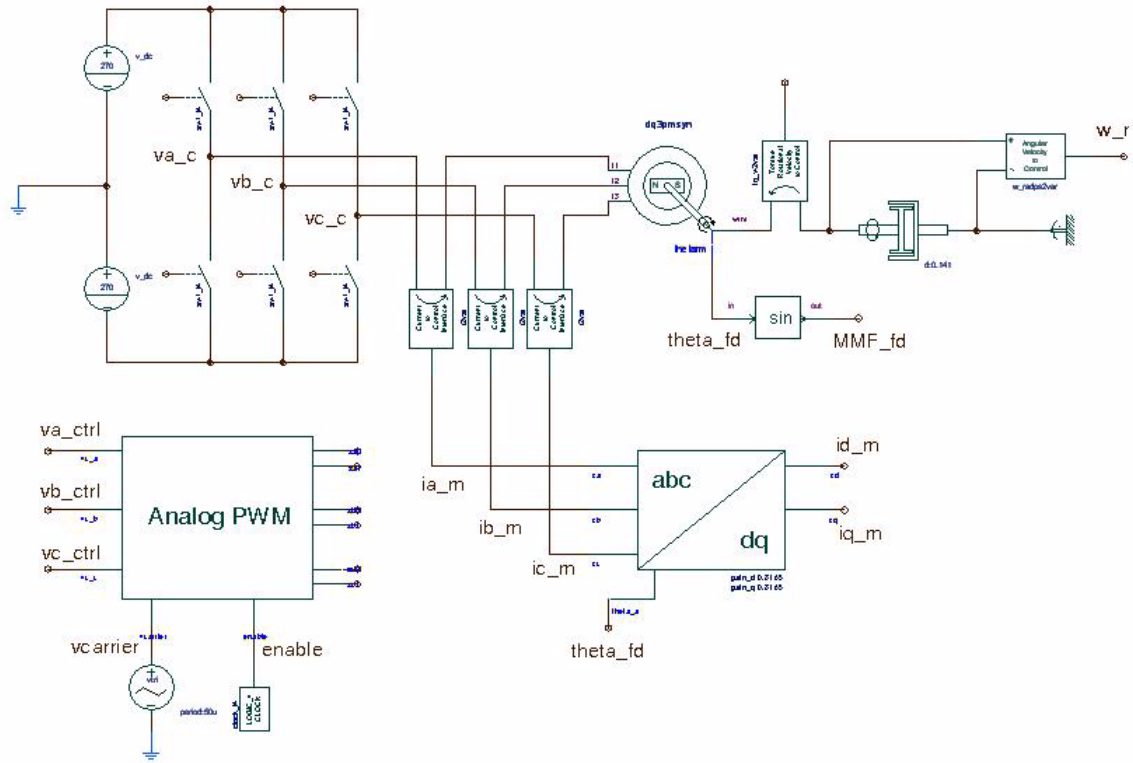


**Fig. 5. 3.** Schematic of VSC with PWM for control of PM motor

## 5.1.4   Model Parameters

The basic parameters for a 20 kW synchronous motor can be found in [26] and are slightly adjusted for the purpose of representing a PM synchronous motor. The VSC switching frequency for this power rating is estimated to be 20 kHz.

**Table 5. 1. Parameters for 20 kW PM Motor for 230 V$_{RMS}$ and 3600 rpm**

| Parameter | Value | Unit |
|:---:|:---:|:---:|
| $r_s$ | 0.1 | $\Omega$ |
| $\psi_{fd}$ | 0.498 | Wb |
| $L_q$ | 4.89 | mH |
| $L_d$ | 2.79 | mH |
| $L_0$ | 0.793 | mH |
| $B$ | 1 | N m rad/s |
| $J$ | 0.01 | kg m$^2$ |
| $P$ | 2 | poles |

Note the rotor of the machine is of salient type, and the q-axis inductance is larger than the d-axis inductance. This is typical for PM motors since the permeability of the magnets is close to that of the air, while the q-axis of the rotor is occupied by iron. The stator resistance corresponds to 3.7% loss. This winding resistance and the motor inertia are copied from the cited reference. The damping torque constant is typically in the order shown.

In addition, the Saber template has provisions for the synchronous reactances to be functions of the stator current in order to model saturation and armature reaction effects; the armature resistance can also model temperature variations. This level of detail will not be included in the implemented models since it falls outside the intended application of system models pursued in this study, where most of the parasitic effects are neglected.

For current controller design based on (8), the PI compensator is sufficient for this application and is designed for high-bandwidth. A high-frequency pole is added for attenuation of switching ripple

$$H_i(s) = \left(K_P + \frac{K_I}{s}\right)\left(\frac{1}{1 + s/\omega_p}\right). \tag{14}$$

The controller crossover frequency was set to 1000 Hz with 79 degrees of phase margin. The corresponding d-axis compensator settings are $K_P = 0.0649$, $K_I = 40.8$ and $\omega_P = 2\pi \cdot 1000$; while for the q-axis $K_P = 0.1138$, $K_I = 71.5$ and $\omega_P = 2\pi \cdot 1000$.

The speed compensator includes two poles at the origin for tracking of ramp control signals in the speed command

$$H_w(s) = \left(K_P + \frac{K_I}{s}\right)\frac{1}{s}. \tag{15}$$

Such improved tracking is required during the acceleration transient of the motor. These two poles at the origin together with the inertial, low-frequency pole given by $(B + D)/J$ limit the bandwidth of the speed control loop to the latter pole frequency since only one zero is used for phase compensation. The mechanical load was set to have $D = 0.141$ Nm/s, and the speed bandwidth as set to 10 Hz with 56 degrees of phase margin, requiring to set $K_P = 159$ and $K_I = 1000$.

## 5.1.5   Validation of Torque and Speed Control Transfer Functions

In order to validate the linear averaged models developed for control of the motor drive, small-signal perturbations are added to circuit while observing the frequency response of selected signals. For example, when a 10%, 100 Hz perturbation is added to the q-axis current reference, the response in the q-axis motor current shall represent the closed loop transfer function in (7). In fact, the bode plot in Fig. 5. 4 shows the correlation of the model (solid-line) and the measured response in Saber (dot).
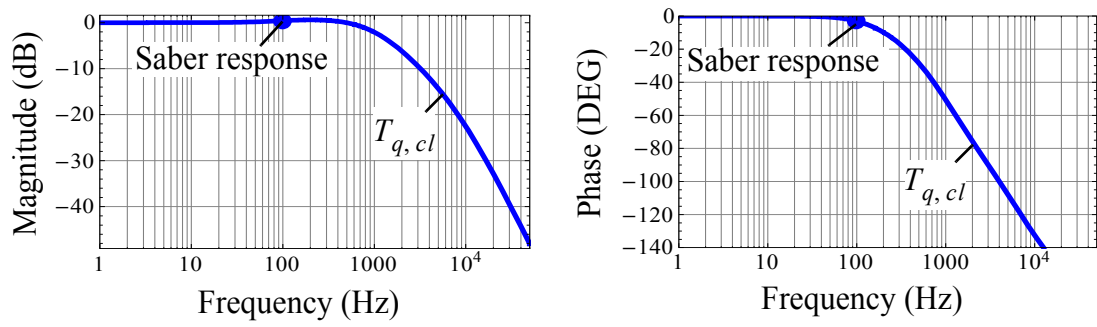
**Fig. 5. 4.** Frequency response of closed loop q-axis current control transfer function.

For the same q-axis reference current perturbation, the measured response of the d-axis motor current was -49 dB, that for all practical purposes reflects the decoupled current control resulting from the feedforward compensation strategy. The decoupling effect of the feedforward compensation scheme is further represented by Fig. 5. 5, where a sudden change in the q-axis reference current has significantly less effect in the system with feedforward compensation.



**Fig. 5. 5.** Time domain response of the dq-coordinate motor currents to a sudden change in the q-axis current command.

62

A perturbation test on the speed command with closed-loop regulation also serves to validate the linear model of the electromagnetic torque. The open-loop transfer function was modeled by (13) and Fig. 5. 6 shows the comparison of the expected closed-loop regulation transfer function (dashed-lines) and the numerical response of the Saber. The perturbation frequency was set to 10 Hz, close to the speed control bandwidth.
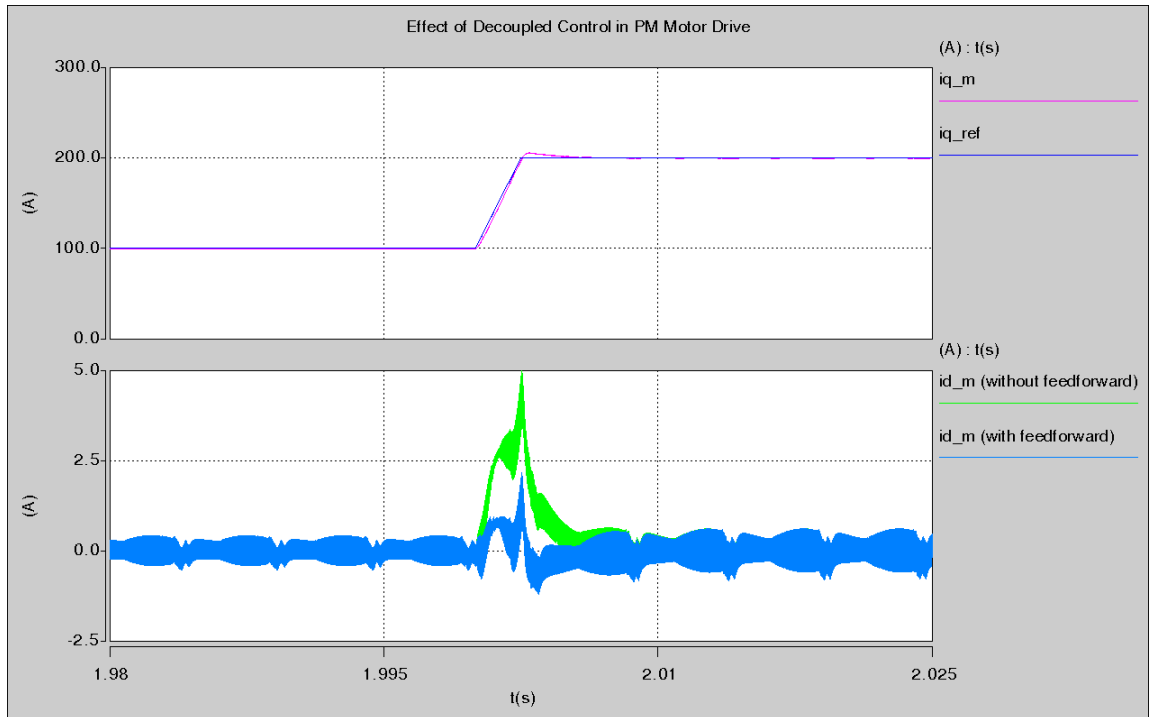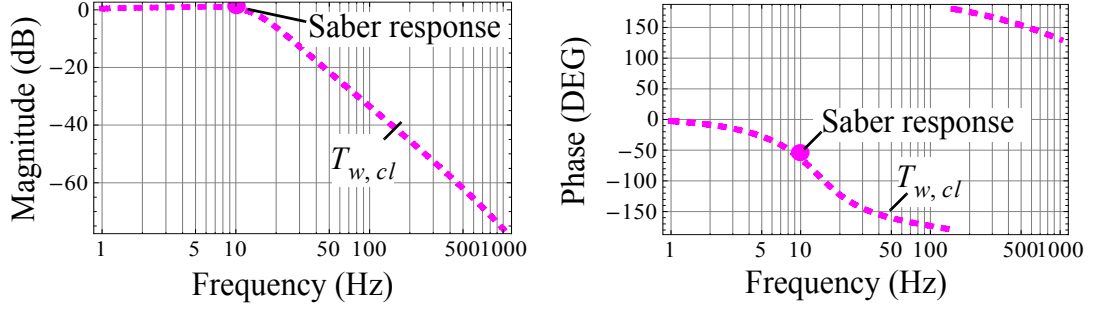


**Fig. 5. 6.** Frequency response of closed loop speed control transfer function.

## 5.1.6 Correlation of Averaged and Switching Models

The averaged model of the VSC is also implemented to drive the PM motor as depicted in Fig. 5. 7. The model corresponds to the switching implementation presented before in Fig. 5. 3. The power input is the dc voltage supply. The negative rail of the dc bus is grounded by a large resistor to provide a reference for model simulation. In an integrated system, the reference to ground is provided by a rectifier circuit. The control inputs are the commanded voltages from the current control loop and the angle information of the motor shaft. The output of the model are the terminals identified with $v_{a,m}$, $v_{b,m}$ and $v_{c,m}$ that shall be connected to the motor terminals, are well as the current signals for feedback control.

Large signal tests are conducted on the averaged model of the motor drive to evaluate its correlation to the switching model. One of the tests consists in the overall transient the motor experiences when accelerated from the stalled position to rated speed and subsequent de-acceleration to a lower speed setting. Fig. 5. 8 presents the time domain response

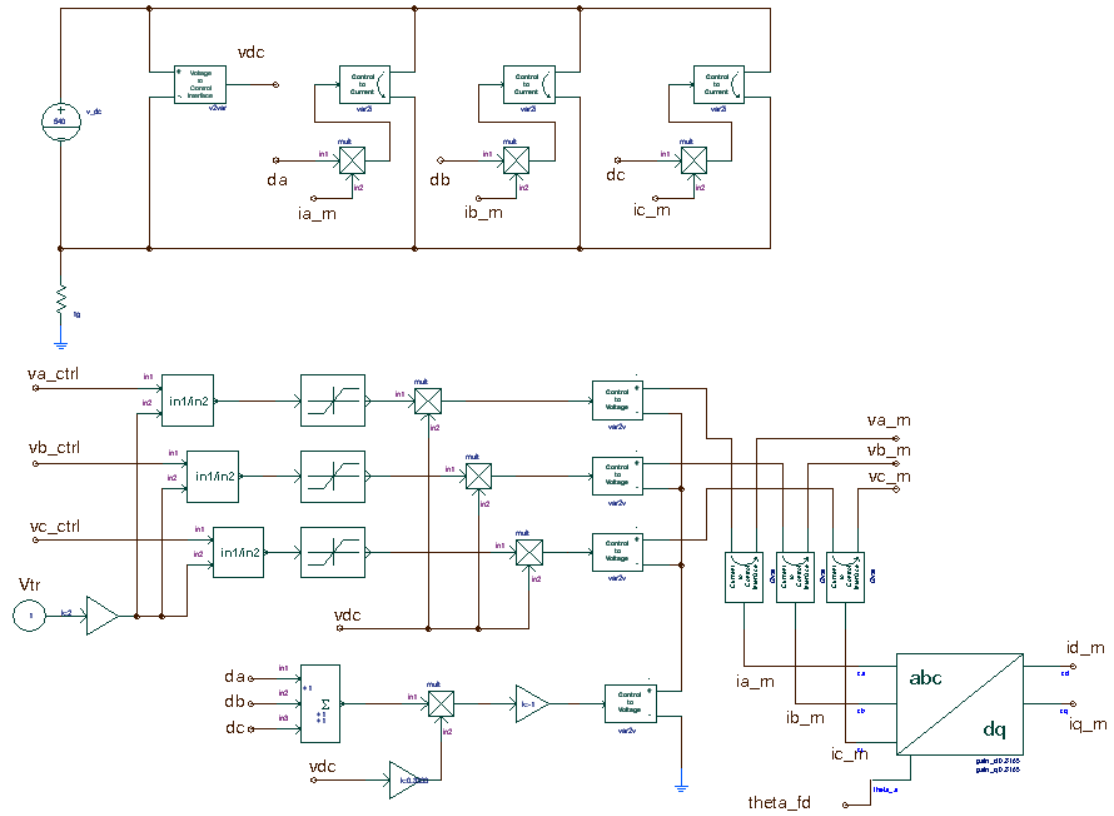**Fig. 5. 7.**  Schematic of the averaged model of the permanent magnet motor drive of the motor speed and phase *a* motor current for the averaged and switching models. The models evidence excellent correlation.
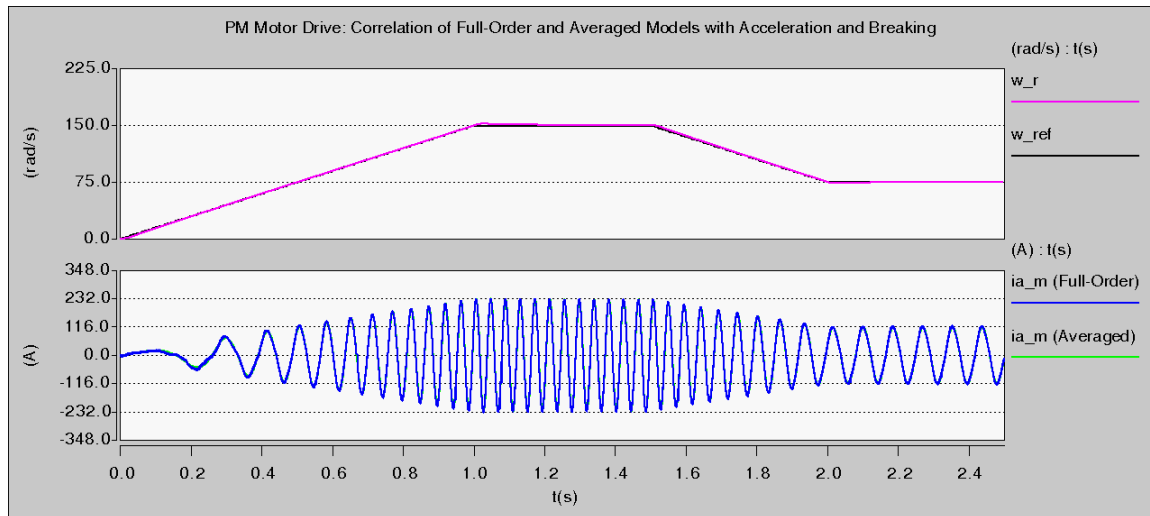


**Fig. 5. 8.**  Time domain response of speed and motor current in averaged and switching models of the permanent magnet motor drive.

An additional large signal test evaluates the correlation of averaged and switching models during the overmodulation period. In Fig. 5. 9, the motor current is commanded to enter the overmodulation region by a step increase in the current control reference. Both averaged and switching models match in this transient period characterized by the nonlinear gain of the modulator.
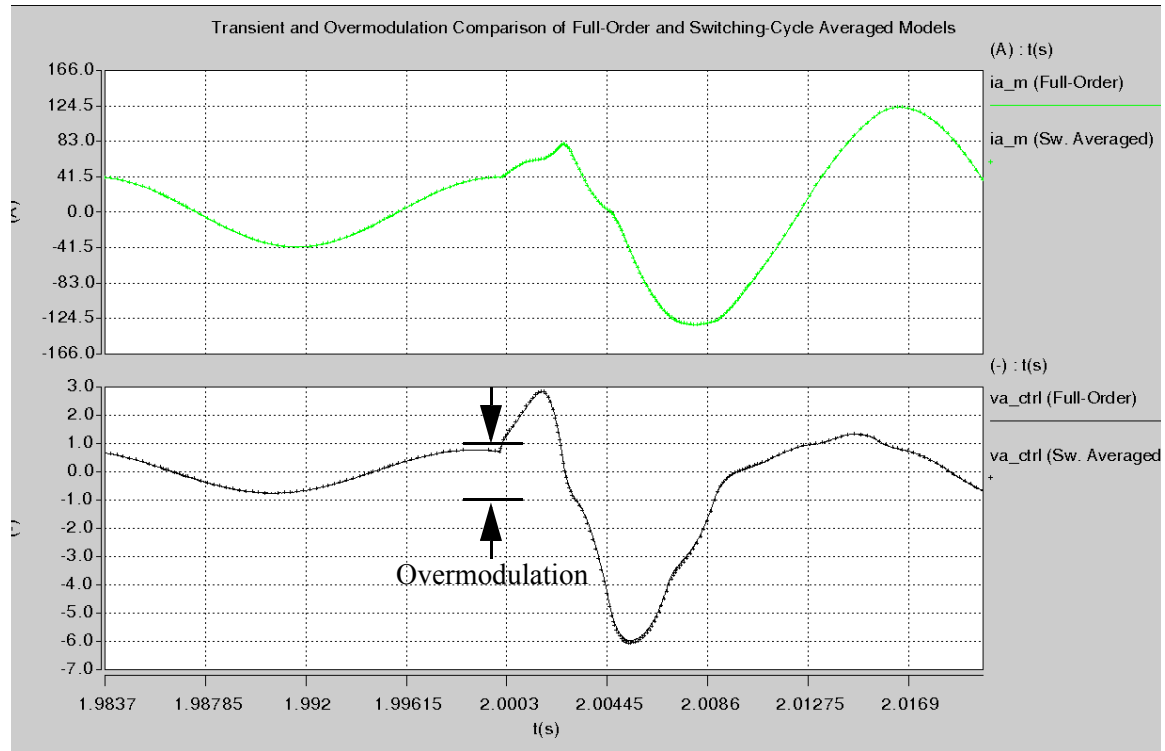


**Fig. 5. 9.** Time domain response of phase *a* motor current during an overmodulation transient in the averaged and switching models of the PM motor drive.

## 5.2 Wounded-Rotor Synchronous Machine Motor Drive

The wounded-rotor synchronous machine template developed initially to perform as a generator will now be used as motor load in a high-power variable frequency motor drive. In fact, the same model parameters representative of the 250 kW turbogenerator will be used here. One of features introduced to the template in Chapter 2 was making the rotor angle information available. This information is particularly useful in trying to align the

stator MMF in quadrature with the rotor MMF so as to achieve maximum torque per ampere control.

## 5.2.1 Drive Modeling and Current Control

Overall, the same control strategy of the PM motor drive applies to the SM drive, but because the SM model includes the presence of damper windings, the specific transfer functions for controller design are different.

The dq-coordinate synchronous generator terminal voltage model is modified by changing the current polarity to follow the motor convention

$$v_d = r_s \cdot i_d - \omega_r \cdot [L_q \cdot i_q + L_{mq}(i_{kq}')] + \frac{d}{dt}[L_d \cdot i_d + L_{md}(i_{fd}' + i_{kd}')]$$

$$v_q = r_s \cdot i_q + \omega_r \cdot [L_d \cdot i_d + L_{md}(i_{fd}' + i_{kd}')] + \frac{d}{dt}[L_q \cdot i_q + L_{mq}(i_{kq}')]$$

$$v_{fd}' = r_{fd}' \cdot i_{fd}' + \frac{d}{dt}[L_{md}i_d + (L_{lfd}' + L_{md})i_{fd}' + L_{md} \cdot i_{kd}'] \qquad . \qquad (16)$$

$$v_{kd}' = r_{kd}' \cdot i_{kd}' + \frac{d}{dt}[L_{md}i_d + L_{md} \cdot i_{fd}' + (L_{lkd}' + L_{md})i_{kd}']$$

$$v_{kq}' = r_{kq}' \cdot i_{kq}' + \frac{d}{dt}[L_{mq}i_q + (L_{lkq}' + L_{mq})i_{kq}']$$

Note the template equations do not need to be changed. The change in current polarity is introduced here just to make the modeling process more intuitive and consequent with the application at hand. Recall $[v_d, v_q]$ and $[i_d, i_q]$ are the stator dq-coordinate voltages and currents respectively. The rotor and damper circuit voltages and currents as referred to the stator circuits are $[v_{fd}', v_{kd}', v_{kq}']$ and $[i_{fd}', i_{kd}', i_{kq}']$ . Resistances and inductances follow the notations introduced before in Chapter 2.

It will be assumed the field current is constant, so that the control strategy resembles the PM motor drive approach in the previous sections. The same control objective is to modify the stator current of the machine to control output torque. However, it is clear the dynamic modeling is slightly more complex due to the presence of damper windings. One

particular simplification in the case of round-rotor synchronous machines is that the d- and q-axis controllers have the same gain settings.

In order to control the motor current, the VSC modifies the machine terminal voltage $[v_d, v_q]$. For control purposes, it is required to develop a frequency domain model of the machine that relates the dynamics of the stator voltage to the stator currents. First it is needed to obtain the damper currents as function of the stator currents, assuming the field current is constant the last two equations in (16) give

$$
\begin{aligned}
I_{kd}{}'(s) &= \left[ \frac{-sL_{md}}{r_{kd}{}' + s(L_{lkd}{}' + L_{md})} \right] I_d(s) \\
I_{kq}{}'(s) &= \left[ \frac{-sL_{mq}}{r_{kq}{}' + s(L_{lkq}{}' + L_{mq})} \right] I_q(s)
\end{aligned}
\tag{17}
$$

The fast current control dynamics are separated from the slow rotor dynamics such that $\omega_r$ is assumed constant in the dq-coordinate stator voltage equations and introducing the result of (17) in the first two equations of (16) gives

$$
\begin{aligned}
V_d(s) &= \left[ r_s + sL_d - \frac{(sL_{md})^2}{r_{kd}{}' + s(L_{lkd}{}' + L_{md})} \right] I_d(s) - \omega_r \left[ L_q - \frac{sL_{mq}^2}{r_{kq}{}' + s(L_{lkq}{}' + L_{mq})} \right] I_q(s) \\
V_q(s) &= \left[ r_s + sL_q - \frac{(sL_{mq})^2}{r_{kq}{}' + s(L_{lkq}{}' + L_{mq})} \right] I_q(s) + \omega_r \left[ L_d - \frac{sL_{md}^2}{r_{kd}{}' + s(L_{lkd}{}' + L_{md})} \right] I_d(s)
\end{aligned}
\tag{18}
$$

The model in (18) shows the coupling between d- and q-axis components. Note there is a missing term $\omega_r L_{md} I_{fd}$ in the q-axis voltage equation because it is a constant which is not relevant in current control.

The averaged modulator model relating the converter voltage $[\bar{v}_d, \bar{v}_q]$ to the inputs of the modulator $[\bar{v}_{d,\,ctrl}, \bar{v}_{q,\,ctrl}]$ and the dc bus voltage $\bar{v}_{dc}$ of the converter was

$$\bar{v}_d = \frac{\bar{v}_{dc}}{2V_{tr}} \bar{v}_{d,ctrl}$$
$$\bar{v}_q = \frac{\bar{v}_{dc}}{2V_{tr}} \bar{v}_{q,ctrl}$$

$$(19)$$

The model is simply a constant gain if the dc voltage is considered constant, which also has slow dynamics compared to those in current control.

The dq-coordinate modulator model of (19) is introduced in (18) to have a complete model for control that relates the input command of the modulator to the machine dq-coordinate currents. The model has the form:

$$V_{d,ctrl}(s) = G_d(s)I_d(s) + \omega_r K_d(s)I_q(s)$$
$$V_{q,ctrl}(s) = G_q(s)I_q(s) + \omega_r K_q(s)I_d(s)$$

$$(20)$$

where

$$G_d(s) = \frac{2V_{tr}}{V_{dc}} \left[ r_s + sL_d - \frac{(sL_{md})^2}{r_{kd}' + s(L_{lkd}' + L_{md})} \right]$$

$$K_d(s) = \frac{2V_{tr}}{V_{dc}} \left[ -L_q + \frac{sL_{mq}^2}{r_{kq}' + s(L_{lkq}' + L_{mq})} \right]$$

$$G_q(s) = \frac{2V_{tr}}{V_{dc}} \left[ r_s + sL_q - \frac{(sL_{mq})^2}{r_{kq}' + s(L_{lkq}' + L_{mq})} \right]$$

$$K_q(s) = \frac{2V_{tr}}{V_{dc}} \left[ L_d - \frac{sL_{md}^2}{r_{kd}' + s(L_{lkd}' + L_{md})} \right]$$

$$(21)$$

The feedforward decoupling strategy has the form

$$V_{d,ctrl}(s) = V_{du,ctrl}(s) + \omega_{ref} K_d(s)I_{q,ref}(s)$$
$$V_{q,ctrl}(s) = V_{qu,ctrl}(s) + \omega_{ref} K_q(s)I_{d,ref}(s)$$

$$(22)$$

where the feedforwad gains in the case of a synchronous machine are not constant as in the PM motor but rather lead-lag networks.

The final closed-loop current control dynamics are described by

$$I_d(s) = \frac{T_{od}(s)}{1 + T_{od}(s)} I_{d, ref}(s) + \frac{G_d^{-1}(s) K_d(s)}{1 + T_{od}(s)} [\omega_r I_q(s) - \omega_{ref} I_{q, ref}(s)]$$

$$I_q(s) = \frac{T_{oq}(s)}{1 + T_{oq}(s)} I_{q, ref}(s) + \frac{G_q^{-1}(s) K_q(s)}{1 + T_{oq}(s)} [\omega_r I_d(s) - \omega_{ref} I_{d, ref}(s)]$$

(23)

where the open loop transfer functions with $H_i(s)$ representing the current compensator are given by

$$T_{od}(s) = H_{id}(s) G_d^{-1}(s)$$
$$T_{oq}(s) = H_{iq}(s) G_q^{-1}(s)$$

(24)

## 5.2.2   Speed Control

For speed control, the torque output has to be expressed as function of the input current. Note the input power to the motor is given by

$$P_{in} = v_d i_d + v_q i_q.$$

(25)

Using the voltage model of the machine in (16), the product of dq-coordinate voltages and currents will contain terms representing resistive losses, terms with the rate of change of the stator currents (inductive energy storage) and terms related to the speed of the rotor. The speed related terms give the airgap power and therefore the electromagnetic torque, given by

$$T_e = L_d i_d i_q + L_{md} I_{fd} i_q + L_{md} i_{kd} i_q - L_q i_q i_d - L_{mq} i_{kq} i_d ,$$

(26)

which can be linearized to give

$$T_e = $$
$$(L_d I_q - L_q I_q - L_{mq} I_{kq}) \hat{i}_d + (L_d I_d + L_{md} I_{fd} + L_{md} I_{kd} - L_q I_d) \hat{i}_q$$
$$+ (L_{md} I_q) \hat{i}_{kd} + (-L_{mq} I_d) \hat{i}_{kq}$$

(27)

69

In the control strategy used here, $i_d$ is commanded to zero. Therefore the terms related to $\hat{i}_d$ and $\hat{i}_{kd}$ are ignored and the model control is simplified significantly. In the frequency domain the electromagnetic model is simply

$$T_e(s) = (L_{md}I_{fd})\hat{i}_q(s) \ . \tag{28}$$

From the mechanical dynamics of the motor shaft

$$T_m = T_e - B\omega_r - J\frac{d\omega_r}{dt}, \tag{29}$$

where $T_m$ is the mechanical torque, $T_e$ is the electromagnetic torque, $B$ and $J$ are the damping and inertial constants of the machine, it is clear the open loop gain of the speed control loop is given by

$$T_{wcl}(s) = \frac{H_w(s)T_{q,cl}(s)L_{md}I_{fd}}{sJ + (B+D)}, \tag{30}$$

where $H_w(s)$ is the speed compensator and $T_{q,cl}(s)$ is the closed-loop current control gain.

### 5.2.3 Model Parameters

For simplicity, the same model parameters representative of the 250 kW turbogenerator will be used for this motor drive application. For the specific settings of the machine parameters please refer to Table 2. 3 in Chapter 2 (page 15). For the motor drive application at hand, it is necessary to specify the field current, its value, as referred to the stator, was set to 2165 A. The inertial load in the shaft of the machine was set to 3 Nm/s.

The current compensator is PI controller with an additional high-frequency pole added to reject noise from the PWM in the current control. The compensator is effectively an integrator in series with a lead-lag network. In addition, because the parameters specify a round-rotor machine both d- and q-axis compensators have equivalent transfer functions given by

$$H_i(s) = \frac{K_I(s/\omega_z + 1)}{s(s/\omega_p + 1)} .$$  (31)

The current control bandwidth is limited by the frequency region where the averaged model of the PWM is valid. Assuming the switching frequency is 10 kHz, the current control bandwidth is set to 1000 Hz and the phase margin is $87.5^o$ when $K_I = 0.31$, $\omega_z = 628\,\text{rad/s}$ and $\omega_p = 62832\,\text{rad/s}$.

The speed compensator is a PI controller with an additional integrator for improved tracking of ramp speed inputs during the acceleration of the motor. The compensator has the form

$$H_w(s) = \frac{(K_P + K_I/s)}{s} .$$  (32)

The speed control bandwidth is limited by the assumption of perfect current regulation, and is set to 4 Hz at full-load with a phase margin of $69.8^o$ when $K_I = 1000$ and $K_P = 159$.

### 5.2.4    Validation of Torque and Speed Control Transfer Functions

The current control model of the motor is validated by inserting a small signal perturbation in the q-axis reference current and observing the response in the q-axis motor current. The response is expected to behave as the closed-loop transfer function which is confirmed by Fig. 5.10.

Validation of the small-signal electromagnetic torque model is done by introducing a small harmonic perturbation in the speed reference and measuring the response of the motor speed at the perturbation frequency. The response is expected to behave as the closed-loop transfer function which is confirmed by Fig. 5.11.

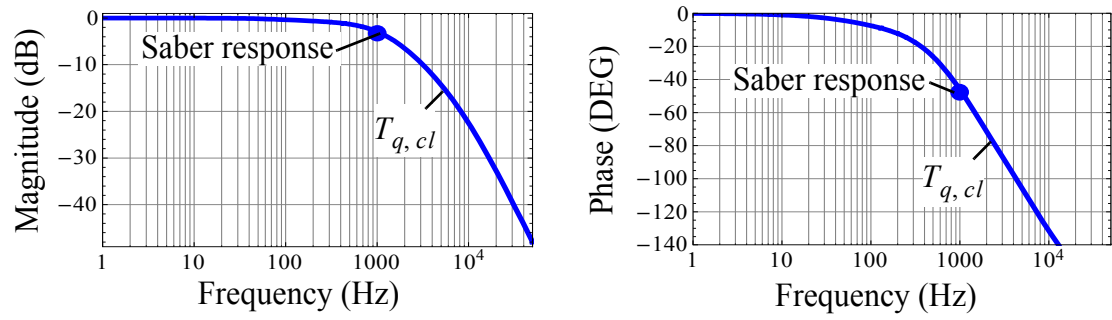**Fig. 5. 10.** Frequency response of the closed-loop transfer function in the q-axis current control of the SM drive.
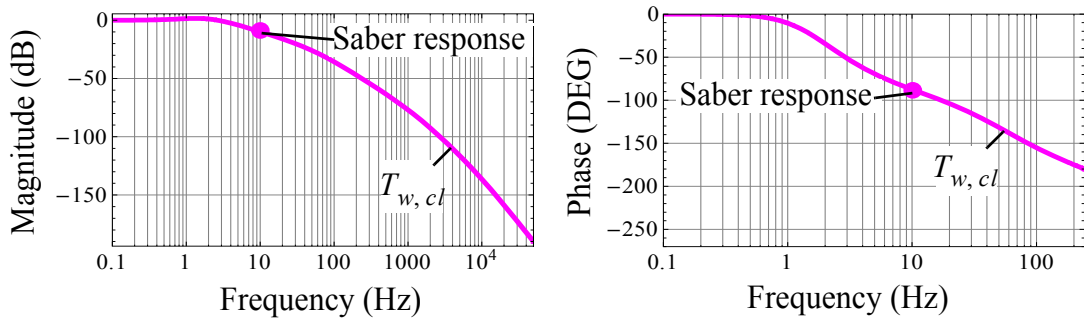


**Fig. 5. 11.** Frequency response of the closed-loop transfer function in speed control of the SM drive.

## 5.3 Conclusions

This Chapter has presented the modeling and control of the permanent magnet and wounded-rotor synchronous machines for variable speed drives. The modeling approach in both types of machines is essentially the same. The VSC averaged model is combined with the motor stator voltage equations to give a combined model of the drive for current control. The speed of the machine is controlled by inflicting changes in the electromagnetic torque, which is the underlying objective in motor drive current control. In both cases, the model for current control is linear if speed and dc voltage are assumed to have much slower dynamics than the stator windings. On the other hand, the electromagnetic torque model for speed control is highly nonlinear involving cross products among stator currents, but conventional small-signal linearization techniques are applicable to the dq-coordinate model of the machines.

There exist however, slight model differences in the specific transfer functions developed for control of the drives. The main reason for this difference stems from the presence of damper windings in the wounded-rotor machine, which are not modelled in the PM motor. This issue makes the dynamics of the wounded-rotor machine a little more complex. For example, the feedforward compensation gain used for decoupling the dynamics of the d- and q-axis current control loops, takes a simple constant value in the PM motor control, but it is otherwise a lead-lag network in the wounded-rotor case.

Another particular difference appears in the implementation of the models for simulation. Because the PM motor template involves a step increase of flux linkages from $t = 0$ to $t = 0^+$, the model requires a very large setting of target iterations in the initialization from zero initial conditions. The problem is alleviated when it is possible to carry a dc analysis for initialization. In the case of the wounded-rotor template, the flux linkages do not experience such discontinuity because the machine is magnetized by a ramp increase of the field excitation current.

The switching and averaged models of the VSC from Chapter 4 have been implemented in motor control. Initial testing on the switching models was done to validate the small-signal transfer functions used in current and speed control. In addition the models were tested to evaluate the capability of the averaged model to follow the dynamics of the switching model. The first of these tests consisted in commanding acceleration and de-acceleration ramps in the speed control of the models, where the correlation was proven accurate. In addition, the models also evidence excellent correlation during an overmodulation transient commanded by the motor current control.

# CHAPTER 6  SUMMARY

This Thesis has presented the development and implementation of digital simulation models of the synchronous generator and switching power converters for the more electric aircraft. Two types of models were developed, namely: 1) full-order models and 2) averaged models.

Chapter 2 has presented the dq-coordinate modeling of the synchronous machine stator and rotor circuits including one damper circuit per rotor axis. The rotor-oriented transformation was introduced to remove the rotor-angle dependency and the model was linearized by assuming constant rotor speed. The model was converted into frequency domain transfer functions that relate the stator voltage response to the field excitation voltage and serve as basis for generator voltage control. Two voltage sensing strategies were evaluated to extract the amplitude voltage information from the three-phase terminals of the generator, the first based on PLL methods and the second based on voltage rectification. Excitation voltage control for regulation of the amplitude of the machine terminal voltage is realized with linear feedback control of the voltage sensed by the dqPLL.

Chapter 3 has presented the design and implementation of representative thirty-pulse and eighteen-pulse ATRU models. The models include the switching action of the line-commutated diodes at the polyphase output of the auto-transformer. The design approach was essentially the same for both converters. The core material selected according to the application. The core size is selected from the power handling ability each application requires. The winding turns are then selected from a volt-per-turn criteria to avoid core saturation. The wire sizes are approximated from their ampere capacity ratings. The more detailed design approach that specifies the wire gauge from the analysis of available winding area has been disregarded. The winding resistances however, are computed from the exact data corresponding to the selected core geometry.

Chapter 4 has presented the switching and averaged model development and implementation for a 2-level PWM VSC. The discontinuous time model of the converter is pre-

sented first and averaging theory is applied subsequently to obtain a continuos time model. The model is still nonlinear, but modeling in an appropriate set of dq-coordinates allows to linearize the model for control purposes. Simulation models are implemented for both the switching and averaged models in Saber. A series of relevant tests are conducted to evaluate the correlation of the models. The dynamic behavior of the state variables in both models evidenced excellent correlation. There still exist limitations on the accuracy of the developed averaged model. One pertaining limitation stems from averaging theory and begins at half the switching frequency of the converter. A second limitation follows from the assumption of balanced three-phase supply in the averaged converter model. Excluding this two possible scenarios, the averaged model of the converter has proven to be a reliable representation of the switching converter during its initialization period, its steady-state equilibrium point and the large perturbation following a dc load removal.

Chapter 5 has presented the modeling and control of the permanent magnet and wounded-rotor synchronous machines for variable speed drives. The modeling approach in both types of machines is essentially the same. The VSC averaged model is combined with the motor stator voltage equations to give a combined model of the drive. There exist however, slight model differences in the specific transfer functions developed for control of the drives. The main reason for this difference stems from the presence of damper windings in the wounded-rotor machine, which are not modelled in the PM motor. This issue makes the dynamics of the wounded-rotor machine a little more complex. The switching and averaged models of the VSC from Chapter 4 have been implemented in motor control. Initial testing on the switching models was done to validate the small-signal transfer functions used in current and speed control. In addition the models were tested to evaluate the capability of the averaged model to follow the dynamics of the switching model. The first of these tests consisted in commanding acceleration and de-acceleration ramps in the speed control of the models, where the correlation was proven accurate. In addition, the models also evidence excellent correlation during an overmodulation transient commanded by the motor current control.

# REFERENCES

[1] P. T. Krein, J. Bentsman, R. M. Bass, and B. L. Lesieutre, "On the use of averaging of power electronic systems," *IEEE Transactions on Power Electronics*, vol. 5, no. 2, pp. 182-190, 1990.

[2] J. Sun and H. Grotstollen, "Averaged modelling of switching power converters: reformulation and theoretical basis," *in Record 23rd Annual IEEE Power Electronics Specialists Conference*, Toledo, Spain, 1992, pp. 1165-1172.

[3] J. Sun and H. Grotstollen, "Symbolic analysis methods for averaged modeling of switching power converters," *IEEE Transactions on Power Electronics*, vol. 12, no. 3, pp. 537-546, 1997.

[4] G. C. Verghese, M. Ilic-Spong, and J. H. Lang, "Modeling and Control Challenges in Power Electronics," in *Proceedings of 25th Conference on Decision and Control*, Athens, Greece, 1986, pp. 39-45.

[5] J. Sun, "Small-Signal Methods for Electric Ship Power Systems," in *Proceedings IEEE Electric Ship Technologies Symposium*, 2009, pp. 44-52.

[6] P. C. Krause, "Synchronous Machines," in *Analysis of Electric Machinery and Drive Systems*, 2nd. ed., New York: IEEE Series, 2002, ch. 5, sec. 5.5, pp. 200-201.

[7] C. Ong, *Dynamic Simulations of Electric Machinery: Using MATLAB/SIMULINK*, Prentice-Hall, 1998.

[8] P. M. Anderson, *Power System Control and Stability*, 2nd. ed., John Wiley & Sons, 2003.

[9] J. Machowski, "Advanced Power System Modeling," in *Power System Dynamics: Stability and Control*, 2nd ed., United Kingdom: John Wiley & Sons, Ltd., 2008, ch. 11, sec. 11.1.1, pp. 434.

[10] J. K. Engelmans, J. R. Wells, E. A. Walters, P. T. Lamm, and M. Daniels, "Development of a Simulation Model for an Aircraft Main Generator," in *Proceedings of 23rd Annual IEEE Applied Power Electronics Conference and Exposition*, Austin, TX, 2008, pp. 1679-1684.

[11] D. W. Novotny and T. A. Lipo, "d,q Modeling of Induction and Synchronous Machines," in

*Vector Control and Dynamics of AC Drives*, New York: Oxford University Press, 2000, ch. 2, pp. 88-102.

[12] Synopsys, *Saber MAST Language User Guide*, Version C-2009.06, June 2009.

[13] *IEEE Recommended Practice for Excitation System Models for Power System Stability Studies*, IEEE Standard 421.5-2005, April 2006.

[14] J. Sun, Z. Bing, and K. J. Karimi, "Small-signal modeling of multipulse rectifiers for more-electric aircraft applications," in *Proceedings of IEEE Power Electronics Specialists Conference*, 2008, pp. 302-308.

[15] K. Furmanczyk and M. Stefanich, "Overview of Multipulse Power Converters for Aerospace Applications," in *Proc. SAE 2008 Power Systems Conference*, Washington, 2008.

[16] R. W. Erickson and D. Maksimovic, *Fundamentals of Power Electronics*, 2nd. ed., New York: Springer Science+Business Media, 2001, ch. 15, pp. 565-584.

[17] W. T. McLyman, *Transformer and Inductor Design Handbook*, 3rd. ed., New York: Marcel Dekker, Inc., 2004.

[18] D. A. Paice, "Optimized 18-pulse type ACIDC, or DCIAC, converter system" U.S. Patent 5 124 904, 1992.

[19] Uan-Zo-li, A.; Burgos, R.; Wang, F.; Boroyevich, D.; Lacaux, F.; Tardy, A, "Comparison of prospective topologies for aircraft autotransformer-rectifier units," in *Proceedings of 29th Annual Conference of the IEEE Industrial Electronics Society*, Virginia, 2003, pp. 1122-1127.

[20] Chivite-Zabalza, F.J.; Forsyth, A.J.; Trainer, D.R., "Analysis and practical evaluation of an 18-pulse rectifier for aerospace applications," in *Proceedings of Second International Conference on Power Electronics, Machines and Drives*, Edinburg, United Kingdom, 2004, pp. 338-343.

[21] Burgos, R.; Uan-Zo-li, A.; Lacaux, F.; Wang, F.; Boroyevich, D.; "Analysis and Experimental Evaluation of Symmetric and Asymmetric 18-Pulse Autotransformer Rectifier Topologies," in *Proceedings of Power Conversion Conference*, Nagoya, 2007, pp. 1286-1293.

[22] J. Sun and K. J. Kamiar, "Small-signal input impedance modeling of line-frequency recti-fiers," *IEEE Transactions on Aerospace and Electronic Systems*, vol. 44, no. 4, pp. 1489-1497, October, 2008.

[23] D. A. Paice, "Optimized 18-pulse type ACIDC, or DCIAC, converter system" U.S. Patent 5 124 904, 1992.

[24] S. Hiti, *Modeling and Control of Three-Phase PWM Converters*, Ph.D. Dissertation, Virginia Polytechnic Institute State University, 1995.

[25] Y. Ye, M. Kazerani, V. Quintana, "Modeling, Control and Implementation of Three-Phase PWM Converters," *IEEE Transactions on Power Electronics*, vol. 18, no. 3, pp.857-864, May, 2003.

[26] D. W. Novotny and T.A. Lipo, *Vector Control and Dynamics of Ac Drives*, New York: Oxford University Press Inc., 1996.

[27] W. Leonhard, "Variable Frequency Synchronous Motor Drives," in *Control of Electrical Drives*, 2nd. ed., New York: Springer, 1996, ch. 14, sec. 14.1, pp. 307-317.

# APPENDIX MODEL LIBRARY AND DESCRIPTION

**Table A.1. Summary of simulation models**

| Component | Description |
|---|---|
| Generator | Synchronous Generator, 250 kW, 400 Hz, 235 $V_{RMS}$ |
| ATRU 30 Pulse | 30 Pulse ATRU, 100 kW, 235 VRMS to 540 V |
| ATRU 18 Pulse | 18 Pulse ATRU, 20 kW, 235 VRMS to 540 V |
| PWM 2 Level Full | Full Order 2 Level PWM Converter, 50 kW, 115 $V_{RMS}$ to 540 V |
| PWM 2 Level Ave | Averaged 2 Level PWM Converter, 50 kW, 115 $V_{RMS}$ to 540 V |
| PM Drive 2 Level Full | Full Order 2 Level Permanent Magnet Motor Drive, 20 kW, 540 V |
| PM Drive 2 Level Ave | Averaged 2 Level Permanent Magnet Motor Drive, 20 kW, 540 V |
| SM Drive 2 Level Ave | Averaged 2 Level Synchronous Machine Drive, 20 kW, 540 V |
| abc2dq & dq2abc | Submodel for abc- to dq- coordinate transformation |
| dqPLL | Submodel for amplitude and phase detection of three-phase voltages |
| Exciter | Submodel representative of IEEE-ST1A |